Mon. Not. R. Astron. Soc. **398,** 1041–1068 (2009) doi:10.1111/j.1365-2966.2009.15082.x

SN 2008S: an electron-capture SN from a super-AGB progenitor?

M. T. Botticella,[1⋆] A. Pastorello,[1] S. J. Smartt,[1] W. P. S. Meikle,[2] S. Benetti,[3] R. Kotak,[1] E. Cappellaro,[3] R. M. Crockett,[1] S. Mattila,[4] M. Sereno,[5] F. Patat,[6] D. Tsvetkov,[7] J. Th. Van Loon,[8] D. Abraham, I. Agnoletto,[3] R. Arbour,[9] C. Benn,[10] G. Di Rico,[11] N. Elias-Rosa,[12] D. L. Gorshanov,[13] A. Harutyunyan,[14] D. Hunter,[1] V. Lorenzi,[14] F. P. Keenan,[1] K. Maguire,[1] J. Mendez,[10] M. Mobberley, H. Navasardyan,[3] C. Ries,[15] V. Stanishev,[16] S. Taubenberger,[17] C. Trundle,[1] M. Turatto[18] and I. M. Volkov[7,19]

[1]*Astrophysics Research Centre, School of Mathematics and Physics, Queen's University Belfast, Belfast BT7 1NN*
[2]*Astrophysics Group, Blackett Laboratory, Imperial College London, Prince Consort Road, London SW7 2BW*
[3]*INAF-Osservatorio Astronomico di Padova, Vicolo dell'Osservatorio 5, 35122 Padova, Italy*
[4]*Tuorla Observatory, Department of Physics & Astronomy, University of Turku, FI-21500 Piikkiö, Finland*
[5]*Institut für Theoretische Physik, Universität Zürich, Winterthurerstrasse 190, CH-8057 Zürich, Switzerland*
[6]*European Southern Observatory (ESO), Karl-Schwarzschild-Str. 2, D-85748, Garching bei München, Germany*
[7]*Sternberg State Astronomical Institute, Universitetskii pr. 13, 119992 Moscow, Russia*
[8]*Astrophysics Group, Lennard-Jones Laboratories, Keele University, Staffordshire ST5 5BG*
[9]*Pennel Observatory, 29 Wrights Way, South Wonston, Hants S021 3He*
[10]*Isaac Newton Group of Telescopes, Apartado 321, E-38700 Santa Cruz de La Palma, Spain*
[11]*INAF-Osservatorio Astronomico di Collurania, Teramo, Italy*
[12]*Spitzer Science Center, California Institute of Technology, 1200 E. California Blvd., Pasadena, CA 91125, USA*
[13]*Central (Pulkovo) Astronomical Observatory, Russian Academy of Sciences, 196140 St Petersburg, Russia*
[14]*Fundación Galileo Galilei-INAF, Telescopio Nazionale Galileo, E-38700 Santa Cruz de la Palma, Tenerife, Spain*
[15]*Universitäts-Sternwarte München, Scheinerstr. 1, 81679 Munchen, Germany*
[16]*Centro Multidisciplinar de Astrofisica, Instituto Superior Tecnico, Av. Rovisco Pais 1, 1049-001 Lisbon, Portugal*
[17]*Max-Planck-Institut für Astrophysik, Karl-Schwarzschild-Str. 1, D-85741 Garching bei München, Germany*
[18]*INAF-Osservatorio Astrofisico di Catania, Via S. Sofia 78, I-95123, Catania, Italy*
[19]*Astronomical Institute of the Slovak Academy of Sciences, 059 60 Tatranska Lomnica, Slovak Republic*

Accepted 2009 May 7. Received 2009 May 7; in original form 2009 March 8

ABSTRACT

We present comprehensive photometric and spectroscopic observations of the faint transient SN 2008S discovered in the nearby galaxy NGC 6946. SN 2008S exhibited slow photometric evolution and almost no spectral variability during the first nine months, implying a long photon diffusion time and a high-density circumstellar medium. Its bolometric luminosity ($\simeq 10^{41}$ erg s^{-1} at peak) is low with respect to most core-collapse supernovae but is comparable to the faintest Type II-P events. Our quasi-bolometric light curve extends to 300 d and shows a tail phase decay rate consistent with that of ^{56}Co. We propose that this is evidence for an explosion and formation of ^{56}Ni ($0.0014 \pm 0.0003\,M_{\odot}$). Spectra of SN 2008S show intense emission lines of Hα, [Ca II] doublet and Ca II near-infrared (NIR) triplet, all without obvious P-Cygni absorption troughs. The large mid-infrared (MIR) flux detected shortly after explosion can be explained by a light echo from pre-existing dust. The late NIR flux excess is plausibly due to a combination of warm newly formed ejecta dust together with shock-heated dust in the circumstellar environment. We reassess the progenitor object detected previously in *Spitzer* archive images, supplementing this discussion with a model of the MIR spectral energy distribution. This supports the idea of a dusty, optically thick shell around SN 2008S with an inner radius of nearly 90 AU and outer radius of 450 AU, and an inferred heating source

⋆E-mail: m.botticella@qub.ac.uk

of 3000 K. The luminosity of the central star is $L \simeq 10^{4.6}\,L_{\odot}$. All the nearby progenitor dust was likely evaporated in the explosion leaving only the much older dust lying further out in the circumstellar environment. The combination of our long-term multiwavelength monitoring data and the evidence from the progenitor analysis leads us to support the scenario of a weak electron-capture supernova explosion in a super-asymptotic giant branch progenitor star (of initial mass 6–8 $M_{\odot}$) embedded within a thick circumstellar gaseous envelope. We suggest that all of main properties of the electron-capture SN phenomenon are observed in SN 2008S and future observations may allow a definitive answer.

Key words: stars: AGB and post-AGB – stars: general – supernovae: general – supernovae: individual: SN 2008S – supernovae: individual: NGC300 OT2008-1 – supernovae: individual: M85 OT2006-1.

1 INTRODUCTION

In recent years, deeper and more frequent searches for transient events and stellar explosions in the local and distant Universe have provided us with important information on the evolution of the most massive stars. However, the simplicity of the emerging picture is compromised by the growing number of peculiar events (e.g. Kulkarni et al. 2007; Quimby et al. 2007; Smith et al. 2007).

From an observational point of view, the challenge is to decide when the introduction of new classes is required or if peculiar or novel transients are just variations of an understood scheme. The discovery of some low-energy events (in terms of their bolometric luminosity and kinetic energies) leads us to investigate in more detail the observational differences between explosive (core-collapse, pair instability explosions) and eruptive (pair instability pulsation, outburst) transients.

From a theoretical point of view, recent observations demonstrate that the standard scenario of stellar evolution and explosion physics may not be complete. Both the extremely bright Type II SNe (Langer et al. 2007; Woosley, Blinnikov & Heger 2007) and the faint Type II SNe (Smith et al. 2009; Berger et al. 2009; Bond et al. 2009) have been proposed to have physical origins other than the core-collapse of a degenerate Fe (or O–Ne–Mg) core.

SN 2008S is one of the most intriguing transient events discovered in recent years. Although it has been given a supernova designation (which we will employ in this paper), it is not yet certain that it was a supernova of the canonical core-collapse type (CCSN). The transient was discovered in NGC 6946 by Arbour & Boles (2008) on February 1.78 UT with a 30-cm f/6.3 Schmidt–Cassegrain reflector at about 17.6 mag. Eight confirming images of SN 2008S were taken on February 2.76 UT, yielding a magnitude of 17.1. Furthermore, Arbour (2008) provided a new image of SN 2008S acquired on 2008 January 24 UT (17.8 mag) and Schmeer (2008) reported an image obtained on 2008 January 30.529 (16.7 mag). The transient was classified as a young reddened Type IIn SN by Stanishev, Pastorello & Pursimo (2008) based on a low-resolution spectrum taken at the Nordic Optical Telescope, with narrow Hβ and Hα emission lines and strong Na I D doublet. Steele et al. (2008) reported a new spectrum of SN 2008S obtained on February 29 UT with the 3-m Shane reflector equipped with Kast double spectrograph at the Lick Observatory, and suggested SN 2008S to be a 'SN impostor' based on peculiar spectral properties and the very faint absolute visual magnitude.

Remarkably, a bright point-like source coincident with SN 2008S was detected in archival *Spitzer* mid-infrared (MIR) images by Prieto et al. (2008b). They found no optical counterpart to this precursor and suggested this MIR source was a stellar progenitor with mass of about 10 $M_{\odot}$ and luminosity of $\sim 3.5 \times 10^4\,L_{\odot}$, enshrouded in its own dust. The stellar mass and the total luminosity estimates result from a blackbody fit to the MIR spectral energy distribution (SED) of the progenitor star. Shortly afterwards, another transient was discovered in the nearby galaxy NGC 300 which bears a striking resemblance to SN 2008S (Berger et al. 2009; Bond et al. 2009). Thompson et al. (2008) reported the discovery of a similar progenitor star in *Spitzer* MIR pre-discovery images and again an optical counterpart was lacking. They suggested that both transients share a common evolutionary channel and also that the optical transient discovered in M85 was of similar origin (Kulkarni et al. 2007; Pastorello et al. 2007). Thompson et al. (2008) and Prieto et al. (2008b) have proposed that these events could be low-energy electron-capture SNe (ECSNe) from stars of initial mass around 9 $M_{\odot}$. The existence of such explosions has been theoretically predicted for many years (Miyaji et al. 1980; Nomoto 1984; Miyaji & Nomoto 1987; Hashimoto, Iwamoto & Nomoto 1993; Kitaura, Janka & Hillebrandt 2006; Poelarends et al. 2008). However, what exactly the mass range of the progenitors would be and how the SN evolution would appear are far from certain. The nature of these transients has not yet been firmly established, since recent works on SN 2008S (Smith et al. 2009) and NGC 300 OT2008-1 (Bond et al. 2009; Berger et al. 2009) suggest that these events are the outbursts of a massive star and not the cataclysmic stellar deaths of stars after core-collapse.

In this paper, we present results from our extensive photometric and spectroscopic follow-up of SN 2008S, together with the analysis of supernova and progenitor observations. The properties of the host galaxy are described in Section 2. Photometric data reduction and analysis are detailed in Section 3 and the evolution of the SED is illustrated in Section 4. Spectroscopic data reduction and analysis are detailed in Section 5. Section 6 is devoted to the analysis of the pre-explosion images and to the discussion of the progenitor star. A summary of our observations, a comparison with other underluminous transients and some Type II-L SNe, and our conclusions on the nature of SN 2008S, are given in Section 7.

2 HOST GALAXY, DISTANCE AND EXTINCTION

SN 2008S was discovered at RA = $20^{\rm h}34^{\rm m}45\overset{\rm s}{.}37$ and Dec. = $60^{\circ}05'58\overset{''}{.}3$ (2000), about 53 arcsec west and 196 arcsec south of

Table 1. Properties of NGC 6946.

α (2000)	$20^{\rm h}34^{\rm m}52\overset{\rm s}{.}3$	1
δ (2000)	$60^\circ09'14''$	1
Galactic longitude	$95\overset{\circ}{.}72$	1
Galactic latitude	$+11\overset{\circ}{.}67$	1
Morphological type	SAB(rs)cd	1
Position angle	242°	2
Inclination angle	$38 \pm 2^\circ$	2
M_B	-21.38 mag	3
L_B	$5.3 \times 10^{10}\,{\rm L}_\odot$	3
Redshift	0.00016 ± 0.000007	1
$v_{\rm Hel}$	48 ± 2 km s^{-1}	1
$v_{\rm galact.}$	275 ± 9km s^{-1}	1
$v^a_{\rm Virgo+GA+Shapley}$	410 ± 19 km s^{-1}	1
Galactic reddening	$E(B-V) = 0.342$ mag	4

1 NASA/IPAC Extragalactic Data base (NED).
2 Boomsma et al. (2008).
3 Carignan et al. (1990).
4 Schlegel et al. (1998).
[a]Based on the local velocity field model given in Mould et al. (2000) using the terms for the influence of the Virgo Cluster, the Great Attractor and the Shapley Supercluster.

the nucleus of NGC 6946. Details of the host galaxy obtained from the NASA/IPAC Extragalactic data base[1] are summarized in Table 1.

Optical, far-infrared, radio continuum and X-ray observations indicate vigorous star formation (SF) throughout the NGC 6946 disc, one of the highest among nearby spiral galaxies, a mild starburst at its centre, and an interstellar medium (ISM) stirred by SNe and stellar winds (Engargiola 1991; Boulanger & Viallefond 1992; Kamphuis & Sancisi 1993; Schlegel 1994; Lacey, Duric & Goss 1997). This high level of SF in the disc of NGC 6946 has been attributed both to its strong spiral density wave (Tacconi & Young 1990) and to stochastic, self-propagating SF (Degioia-Eastwood et al. 1984). Signs of low-level SF such as H II regions and UV bright clusters have been discovered in the far outer regions of galactic disc well beyond the R_{25} radius.

Eight other SNe have been detected in this galaxy six of which were classified as Type II SNe [1917A (II), 1948B (II-P), 1968D (II), 1980K (II-L), 2002hh (II-P), 2004et (II-P)] and two remain unclassified (SN 1939C and SN 1969P). All these SNe were brighter than mag 15 except SN 2002hh which was highly reddened. Among these eight SNe, four have been detected as radio SNe (1968D, 1980K, 2002hh, 2004et) and three as X-ray SNe (1968D, 1980K, 2004et). Many SN remnants have been detected in NGC 6946 using optical, radio and X-ray telescopes (Matonick & Fesen 1997; Schlegel, Blair & Fesen 2000; Pannuti, Schlegel & Lacey 2007).

2.1 Metallicity

The galactic metallicity at the position of SN 2008S can be estimated in a similar way to that for two other recent SNe in this galaxy (SN 2002hh and SN 2004et) as shown by Smartt et al. (2009). The abundance gradient determined by Pilyugin, Vílchez & Contini (2004) [$12 + \log {\rm O/H} = 8.7 - 0.41(R/R_{25})$] and the de-projected galactocentric radius of the SN position can be used to determine the likely local metallicity at the position of SN 2008S. Using the distance of 5.7 Mpc as discussed in Section 2.2, SN 2008S is at a deprojected galactocentric radius of 4.9 kpc, and with $R_{25} = 9.1$ kpc (from HyperLeda,[2] Paturel et al. 2003), the metallicity gradient of Pilyugin et al. (2004) results in an approximate oxygen abundance of 8.5 dex. On the Pilyugin et al. (2004) abundance scale, solar is approximately 8.7 dex. Hence, the environment of SN 2008S is mildly sub-solar, although within the uncertainties in this method a solar-like composition of the progenitor is still quite possible. By comparison, the oxygen abundances estimated for SN 2002hh and SN 2004et are approximately 8.5 and 8.3 dex, respectively (Smartt et al. 2009).

2.2 Distance

There are several estimates of the distance to NGC 6946, obtained with different methods and listed in Table 2. Two SNe hosted in NGC 6946 have been used as distance indicators. Schmidt et al. (1994) applied the Expanding Photosphere Method (EPM) to SN 1980K and found a distance modulus of 28.78 ± 0.4 mag. Sahu et al. (2006) used a 'standard candle method' (SCM) for SN 2004et, based on the correlation between the expansion velocities of the SN II-P ejecta and the bolometric luminosities during the plateau phase (Hamuy & Pinto 2002; Nugent et al. 2006). They obtained $\mu = 28.78 \pm 0.11$ mag, in close agreement with the estimate obtained with EPM for SN 1980K. There is one distance estimate that is significantly different from the rest: the radio observations of SN 1980K yield a much larger value of 30.5 ± 0.3 Mpc (Weiler et al. 1998). As this is much larger than the other estimates (which are consistent within the uncertainties), we shall discount this value and use an unweighted mean of 28.78 ± 0.08 mag throughout this paper.

2.3 Extinction

NGC 6946 is located close to the Galactic plane (Galactic latitude $\sim 12^\circ$), with an estimated reddening of $E(B-V) = 0.342$ mag (Schlegel, Finkbeiner & Davis 1998). For the SNe which occurred in this galaxy, different values of extinction have been estimated depending on the SN position. In all cases, the presence of the Na I D ($\lambda\lambda$5890,5896) lines has been used as an indicator of the presence of dust and used to estimate the reddening at the SN position (Zwitter, Munari & Moretti 2004; Meikle et al. 2006; Sahu et al. 2006; Pozzo et al. 2006). Strong Na I D lines in absorption are also present in the SN 2008S spectra until about 70 d after the explosion. The EW(Na I D) appears to show a temporal evolution from 4.4 to 2.5 Å during this time (Table 3 and Fig. 1).

To estimate the error in our equivalent width (EW) measurements, we performed a Monte Carlo simulation adding a number of absorption lines with known EW at different positions in each SN spectrum and re-measured their EW. We repeated the simulation for different values of line EW and strength. These simulations were performed separately in each spectrum to take account of the differences in spectral resolution and signal-to-noise ratio (S/N). In order to investigate the reality of the EW changes in the Na I D lines, we carried out a quantitative statistical test, performing a linear fit to the data, and found a negative slope at the 2σ (95 per cent confidence) level. To test further that the data are better represented by a temporally declining EW, rather than a fixed value, we exploited the Bayesian information criterion (BIC), which give an approximation for the Bayes factor (see Liddle 2004, and references therein). The BIC is defined as $\chi^2 + N_{\rm par} \log N_{\rm data}$ where χ^2 is the total χ^2

[1] NASA/IPAC Extragalactic Data base, http://nedwww.ipac.caltech.edu/

[2] HYPERLEDA data base, http://leda.univ-lyon1.fr

Table 2. Estimates of the distance to NGC 6946.

Distance (Mpc)	Distance modulus (mag)	Method	Reference
5.5	28.70	HI Tully–Fisher relation	Pierce (1994)
5.4	28.66	CO Tully–Fisher relation	Schoniger & Sofue (1994)
6.0 ± 0.5	28.90 ± 0.18	Galaxy brightest supergiants	Sharina, Karachentsev & Tikhonov (1997)
5.9 ± 0.4	28.85 ± 0.15	Brightest supergiants of group	Karachentsev, Sharina & Huchtmeier (2000)
5.6 ± 1.8	28.73 ± 0.68	'Sosie galaxies'	Terry, Paturel & Ekholm (2002)
6.1 ± 0.6	28.92 ± 0.21	Planetary nebulae luminosity function	Herrmann et al. (2008)
5.7 ± 0.7	28.78 ± 0.40	EMP SN 1980K	Schmidt et al. (1994)
5.7 ± 0.3	28.78 ± 0.11	SCM SN 2004et	Sahu et al. (2006)

Table 3. Measurements of the EW of Na I D.

JD[a]	Ph[b]	EW (Å)
501	16	4.4 ± 0.50
504	19	3.4 ± 0.45
508	22	3.2 ± 0.45
514	28	2.7 ± 0.35
524	38	2.5 ± 0.48
530	44	2.5 ± 0.40
533	47	2.3 ± 0.48
554	68	2.6 ± 0.48

[a]JD − 245 4000.00.
[b]Phase is in days after the explosion date JD 245 4486 ± 4.

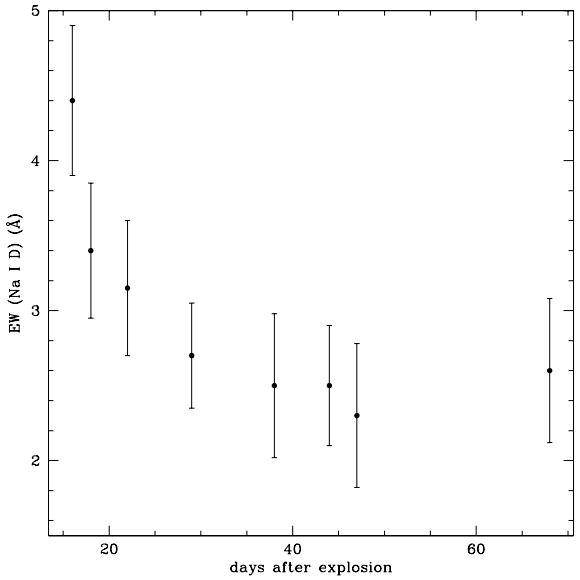

Figure 1. Temporal evolution of the EW(Na I D). Phase is in days after the explosion epoch (JD 245 4486).

for the model, $N_{\rm par}$ is the number of parameters of the model and $N_{\rm data}$ is the number of data points used in the fit. The best model minimizes the BIC. A difference of 2 for the BIC is regarded as positive evidence, and of 6 or more as strong evidence, against the model with the larger value. The BIC corresponding to no evolution is larger by 6 than the BIC for a straight line with slope ($\Delta{\rm BIC} = {\rm BIC}_{\rm const} - {\rm BIC}_{\rm slope} > 6$), clearly supporting the scenario for a decreasing temporal evolution. The two BIC values are comparable only if we exclude from the analysis the first two epochs. We conclude that we find evidence for a change in EW of the Na I D feature.

The evolution of the local component EW(Na I D) may be due to an evolution of the ionization conditions in the circumstellar material (CSM) and in the ejecta of SN 2008S since the EW is related to the ionization stage of Na I. The evolution in the EW may also imply that the local extinction underwent a temporal decline. However, given (a) the lack of any well-established EW(Na I D)-exinction correlation at the very large EWs involved, and (b) the possibility that the Na I D feature includes saturated components, we make no attempt to use the EW(Na I D) to determine the extinction or its possible variation. In any case, the EW(Na I D) variation could be simply due to the evolution of the physical properties of the gas around SN 2008S (see Section 5.2), with the extinction taking place at a completely different location. By days 182 and 256, the Na I D feature has become visible in emission. This change is also indicative of the circumstellar origin of this feature.

The presence of circumstellar Na I D has also been observed in the Type IIn SN 1998S and has been interpreted as a signature of slow-moving outflows originating from the progenitor while its blueshift and growing intensity between 20 and 40 d after explosion has been associated with variable physical conditions in the CSM (Bowen et al. 2000). Chugai & Utrobin (2008) studied the formation of the Na I D and Ca II H&K lines in the red supergiants (RSG) wind after an SN II-P explosion with the goal of using these as a diagnostic of the wind density. They extrapolated their model to a very high wind density to reproduce the intensity of these lines observed in SN 1998S. However, the EW of the absorption depends non-monotonically on the wind density. The case of SN 1998S with its very dense wind has shown that the EW(Na I D) decreases with wind density because of the ionization of metals in the wind by UV radiation. Variable EW(Na I D) has been detected also in a few Type Ia SNe (2006X, Patat et al. (2007); 1999cl, Blondin et al. (2009); 2007le, Simon et al., in preparation). However, this does not seem to be a very common phenomenon (Blondin et al. 2009), and the interpretation in terms of evolution of the CSM physical conditions induced by the SN radiation field (Patat et al. 2007) is still debatable (Chugai 2008).

Here, we adopt the Galactic absorption in V band, $A_V = 1.13$ mag, calculated from the list of $A/E(B-V)$ of Schlegel et al. (1998) along with their estimate of $E(B-V)$ and an extinction local to the SN, $A_V \sim 1$ mag, required by our light-echo model to fit the observed SED at 17 d after explosion when the MIR excess is observed (see Section 4.1). If we assume $A_V = 2.13$ mag, the EW of K I (λ7699) would be about 0.17 Å following the calibration by Munari & Zwitter (1997). Unfortunately, the K I region of the spectrum lies close to strong telluric absorption (7570–7750 Å) and is only ever covered at low resolution so we did not observe the K I feature.

Table 4. Summary of the characteristics of the telescopes used during the photometric follow up.

Telescope	Primary mirror (m)	Camera	Array	CCD	Pixel scale (arcsec pixel^{-1})	Field of view (arcmin)	Filters
TNGD	3.6	DOLORES	2048 × 2048	EEV 42-40	0.25	8.6 × 8.6	Johnson *U*, *B*, *V*; Cousin *R*, *I*
TNGN	3.6	NICS	1024 × 1024	HgCdTe Hawaii	0.25	4.2 × 4.2	*JHK*
NOT	2.5	ALFOSC	2048 × 2048	EEV 42-40	0.19	6.4 × 6.4	Johnson *U*, *B*, *V*, *R*
CAHAT	2.2	CAFOS	2048 × 2048	SITe	0.53	16 × 16	Johnson *B*, *V*, *R*, *I*
LT	2.0	RATCam	2048 × 2048	EEV 42-40	0.13	4.6	Bessel *U*, *B*, *V*; Sloan r', i'
CAO	1.8	AFOSC	1024 × 1024	TK1024AB	0.46	7.8	Bessel *B*, *V*, *R*; Gunn *i*
SAO	1.0		2048 × 2048	EEV 42-40	0.48	8.3	Johnson *V*
AZT24	1.0	SWIRCAM	256 × 256	HgCdTe PICNIC	1.03	4.4	*JHK*
MSK	0.7	Apogee AP-7p	512 × 512	SITe	0.94	4	Johnson *B*, *V*, *I*; Cousin *R*
MSKL	0.7	Apogee AP-7p	512 × 512	SITe	0.64	5.5	Johnson *B*, *V*, *I*; Cousin *R*
CRM	0.6	Apogee AP-47p	1024 × 1024	Marconi47-10	0.71	6.1	Johnson *B*, *V*, *I*; Cousin *R*
SLV	0.5	SBIG ST-10XME	2184 × 1472	KAF3200ME	1.12	20.6 × 13.9	Johnson *B*, *V*; Cousin *R*, *I*
WOT	0.4	SBIG ST-10 XME	2184 × 1472	KAF3200ME	0.44	16.0 ×10.8	Sloan r'

TNGD = the Telescopio Nazionale Galileo (TNG) with the Device Optimized for the LOw RESolution (DOLORES); TNGN = the Telescopio Nazionale Galileo (TNG) with the Near-Infrared Camera Spectrometer (NICS); NOT= the Nordic Optical Telescope (NOT) with the Andalucia Faint Object Spectrograph and Camera (ALFOSC); CAHAT = the 2.2-m telescope at Calar Alto Observatory (CAHA) with the Calar Alto Faint Object Spectrograph (CAFOS); LT = the Liverpool Telescope (LT) with the optical CCD camera RATCam; CAO = the Copernico telescope at Asiago Observatory with the Asiago Faint Object Spectrograph and Camera (AFOSC); SAO = the 1-m telescope of Special Astrophysical Observatory of Russian Academy of Sciences; AZT24 = the AZT 24 telescope at Campo Imperatore Observatory with SWIRCAM; MSK = the 70 cm telescope of the Sternberg Astronomical Institute in Moscow; MSKL = the 70 cm telescope of the Sternberg Astronomical Institute +focal reducing lens; CRM = the 60 cm reflector of the Sternberg Astronomical Institute Crimean laboratory; SLV = the 50 cm telescope of the Astronomical Institute of Slovak Academy of Sciences at Tatranska Lomnica; WOT = the 40 cm telescope at the Wendelstein Observatory.

3 PHOTOMETRIC DATA AND ANALYSIS

We commenced monitoring SN 2008S shortly after the discovery epoch and collected data for the following eight months with a sampling rate among the highest ever obtained for such a peculiar transient. Data obtained before the discovery date by several amateur astronomers are also included to constrain the explosion epoch of SN 2008S. The unfiltered image acquired by D. Abraham on January 16 (JD 245 4482) shows no object visible in the SN 2008S location with a limiting magnitude of 19.20 in *V* band (18.60 in *R* band), while the first detection of SN 2008S is 8 d later on January 24 (JD 245 4490). We therefore adopt January 20 (JD 245 4486) as the explosion epoch, the uncertainty being about 4 d. The phases in this paper are relative to the explosion date (when we fix ph=0).

3.1 Optical data

Optical photometry of SN 2008S was obtained with many telescopes and a summary of their characteristics is given in Table 4. Unfiltered images were obtained for many epochs with a 40 cm telescope with a SXVF-H9 camera, a 30 cm telescope with a MX916 camera, a 35 cm telescope with a ST-9E/9XE camera and with a 25 cm telescope with a ICX424 CCD.

Basic data reduction (overscan correction, bias subtraction, flat fielding, trimming) was performed using standard routines in IRAF.[3] The instrumental magnitudes were obtained with the point spread function (PSF) fitting technique using a custom made DAOPHOT based package (SNOOPY). We did not apply the template subtraction technique, since the host galaxy contamination is negligible around SN 2008S in the optical and in the near-infrared (NIR) range.

[3] Image Reduction and Analysis Facility (IRAF) is distributed by the National Optical Astronomy Observatories, which are operated by the Association of Universities for Research in Astronomy, Inc., under cooperative agreement with the National Science Foundation.

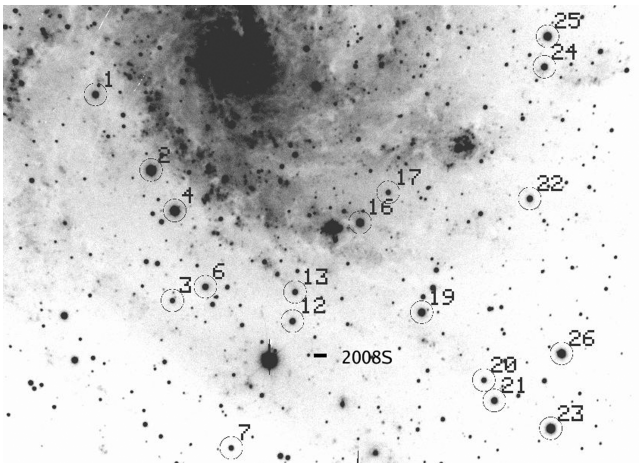

Figure 2. Finding chart for the local sequence of stars employed for the optical photometric calibration. The numbers are adopted from Pozzo et al. (2006).

The photometric calibration was carried out by a comparison with Landolt standard stars observed the same night when possible. As our local sequence of stars, we chose a subset of that adopted in Pozzo et al. (2006) for SN 2002hh, shown in Fig. 2 and calibrated it with respect to a number of Landolt standard fields on several photometric nights.

Our calibration is in agreement with that of Pozzo et al. (2006) with an average difference of 0.01 mag in the *V* and *I* bands and of 0.005 mag in the *R* band. The magnitudes of the calibrated local sequence, listed in Table A1, were subsequently used to measure the relative SN 2008S magnitude for each observation. The *UBVRI* magnitudes of SN 2008S are reported with their uncertainties estimated by combining in quadrature the error of the photometric calibration and the error in the PSF fitting in Table 5. The responses of the SXVF-H9 camera used by A. Arbour, and the ST-9E/9XE

Table 5. Optical, NIR and unfiltered photometry of SN 2008S.

JD[a]	Ph[b]	*U*	*B*	*V*	*R*	*I*	*J*	*H*	*K*	Instrument
490.3	4			17.25 ± 0.20	16.66± 0.50					MX916+ ICX424 unfiltered
498.3	12			16.97 ± 0.30						MX916 unfiltered
501.3	15			16.95 ± 0.08	16.34 ± 0.05					SXVF-H9+ST-9E/9XE unfiltered
501.4	15				16.35 ± 0.01					NOT
502.2	16		17.92 ± 0.16	16.87 ± 0.12	16.32 ± 0.08	15.87 ± 0.07				MSK
503.3	17			16.88 ± 0.10	16.39 ± 0.05					SXVF-H9+ST-9E/9XE unfiltered
505.3	19			16.98 ± 0.14	16.33 ± 0.06					SXVF-H9+ST-9E/9XE unfiltered
506.3	20				16.26 ± 0.06					SXVF-H9+ST-9E/9XE unfiltered
507.8	22	17.89 ± 0.04	17.77 ± 0.03	16.91 ± 0.01	16.35 ± 0.02	15.79 ± 0.02				TNGD
508.3	22			17.10 ± 0.14	16.36 ± 0.06					SXVF-H9+ST-9E/9XE unfiltered
508.7	23		17.81± 0.30	16.90 ± 0.50	16.37 ± 0.04	15.86 ± 0.07				CAHAT
509.3	23			17.12 ± 0.14	16.44 ± 0.11					SXVF-H9+ST-9E/9XE unfiltered
510.3	24			17.10 ± 0.14						SXVF-H9 unfiltered
512.3	26			17.08 ± 0.12	16.42 ± 0.09					SXVF-H9+ST-9E/9XE unfiltered
514.3	28			16.99 ± 0.13						SXVF-H9 unfiltered
514.7	29		17.91 ± 0.03	17.00 ± 0.01	16.48 ± 0.01	15.91 ± 0.01				CAO
515.3	29			17.06 ± 0.40						SXVF-H9 unfiltered
515.8	30	18.26 ± 0.10	17.89 ± 0.03	17.01 ± 0.02	16.47 ± 0.01	15.91 ± 0.01				LT
517.3	32				16.52 ± 0.08	16.03 ± 0.13				MKS
522.7	37		17.98 ± 0.01	17.10 ± 0.01	16.57 ± 0.01	16.11 ± 0.02				CAHAT
523.2	37		18.15 ± 0.14	17.08 ± 0.07	16.61 ± 0.04	16.20 ± 0.06				MSK
523.3	37			17.05 ± 0.08	16.54 ± 0.07					SXVF-H9+ST-9E/9XE unfiltered
524.7	39	>18.70	18.04 ± 0.06	17.18 ± 0.02	16.67 ± 0.02	16.10 ± 0.01				LT
525.7	40			17.13 ± 0.06						SXVF-H9 unfiltered
526.8	41						15.20 ± 0.09	15.16 ± 0.09	14.95 ± 0.1	TNGN
528.7	43			17.22 ± 0.11						SXVF-H9 unfiltered
530.3	44			17.25 ± 0.12						SXVF-H9 unfiltered
530.8	45	18.90 ± 0.15	18.22 ± 0.05	17.37 ± 0.03	16.75 ± 0.03	16.20 ± 0.02				LT
532.7	47		18.39 ± 0.02	17.38 ± 0.01	16.83 ± 0.01	16.26 ± 0.02				CAHAT
533.3	47				16.65 ± 0.11					ST-9E/9XE unfiltered
537.6	52		18.46 ± 0.11	17.46 ± 0.05	16.91 ± 0.03	16.45 ± 0.04				SLV
539.7	54		18.59 ± 0.01	17.57 ± 0.02	16.99 ± 0.02	16.41 ± 0.01				LT
543.6	57				17.15 ± 0.05	16.55 ± 0.05				SLV
544.7	59				17.14 ± 0.04					NOT
546.6	61			17.88 ± 0.14	17.27 ± 0.10	16.70 ± 0.07				SLV
546.7	61						15.75 ± 0.10			AZT24
554.2	68		19.25 ± 0.08	17.96 ± 0.01	17.35 ± 0.02	16.70 ± 0.01				LT
555.5	69				17.31 ± 0.21					SLV
556.6	71			18.18 ± 0.09	17.44 ± 0.04	16.81 ± 0.05				SLV
556.6	71						16.00 ±0.09	15.62 ± 0.09	15.39 ± 0.15	AZT24
556.7	71		19.30 ± 0.09	18.16 ± 0.02	17.43 ± 0.01	16.78 ± 0.01				CAO
557.7	72			18.15 ± 0.04	17.43 ± 0.04	16.77 ± 0.03				LT
570.7	84	20.92 ± 0.10	20.16 ± 0.07	18.63 ± 0.03	17.82 ± 0.02	17.11 ± 0.01				LT
572.7	86	20.93 ± 0.14	20.17 ± 0.04	18.78 ± 0.02	17.87 ± 0.01	17.16 ± 0.01				LT
573.6	87	20.93 ± 0.30	20.18 ± 0.09	18.79 ± 0.03	17.90 ± 0.01	17.14 ± 0.01	16.32 ±0.08	15.96 ± 0.08	15.65 ± 0.09	TNGD,TNGN
574.6	88		20.13 ± 0.07	18.83 ± 0.03	18.03 ± 0.02	17.20 ± 0.02				LT
576.6	90		20.34 ± 0.14	18.82 ± 0.04	18.10 ± 0.03	17.32 ± 0.01				LT
577.6	91	21.01 ± 0.30	20.36 ± 0.01	18.97 ± 0.03	18.12 ± 0.02	17.33 ± 0.02				LT
579.5	93			19.10 ± 0.10	18.18 ± 0.10	17.33 ± 0.07				MSKL
582.6	96			19.15 ± 0.05						CAHAT
585.4	99			19.24 ± 0.30	18.35 ± 0.09	17.54 ± 0.08				MSKL
590.4	105				18.45 ± 0.11	17.67 ± 0.10				MSKL
590.7	105			19.51 ± 0.01	18.55 ± 0.01					LT
592.6	107		20.88 ± 0.09	19.57 ± 0.06	18.61 ± 0.03	17.80 ± 0.02				CAO
593.6	108	21.68 ± 0.20	21.07 ± 0.13	19.65 ± 0.05	18.67 ± 0.02	17.82 ± 0.02				TNGD
601.5	115				19.10 ± 0.2					WOT
602.2	116			20.06 ± 0.09	19.15 ± 0.04					LT
602.5	117				19.17 ± 0.47					MSKL
604.5	118				19.28 ± 0.37	18.10 ± 0.26				CRM
607.5	122			20.26 ± 0.26						CRM
607.7	122			20.27 ± 0.06	19.26 ± 0.04					LT
608.1	123			20.25 ± 0.11	19.35 ± 0.05					LT
613.4	127				19.39 ± 0.19	18.45 ± 0.15				MSKL
618.5	132			20.58 ± 0.21						SAO
619.5	133				19.45 ± 0.20					WOT
621.5	135			20.65 ± 0.27	19.49 ± 0.20	18.55 ± 0.08				CAO
627.6	142			20.93 ± 0.13	19.67 ± 0.07					LT

Table 5 – *continued*

JD[a]	Ph[b]	*U*	*B*	*V*	*R*	*I*	*J*	*H*	*K*	Instrument
629.6	144						17.68 ±0.06	16.72 ± 0.05	16.12 ± 0.05	TNGN
637.4	151			20.94 ± 0.14	19.87 ± 0.06	18.95 ± 0.03				LT
642.6	157			21.01 ± 0.21	19.94 ± 0.07	19.05 ± 0.04				LT
646.6	159		22.47 ± 0.22	21.08 ± 0.14	20.05 ± 0.09					CAHAT
648.4	162			21.18 ± 0.30	20.02 ± 0.07	19.07 ± 0.07				LT
651.5	165			21.30 ± 0.30	20.06 ± 0.05	19.07 ± 0.05				LT
658.5	172			21.34 ± 0.28	20.15 ± 0.08	19.13 ± 0.05				LT
659.5	174						17.77 ±0.06	16.75 ± 0.08	16.05 ± 0.08	TNGN
667.5	181				20.21 ± 0.26	19.24 ± 0.32				LT
672.4	186			21.52 ± 0.15	20.27 ± 0.05	19.34 ± 0.05				LT
677.4	191			21.53 ± 0.23	20.28 ± 0.06	19.33 ± 0.04				LT
697.5	212						17.99 ±0.10	16.78 ± 0.09	16.00 ± 0.08	TNGN
714.4	228			22.09 ± 0.30	20.75 ± 0.11	19.65 ± 0.10	18.14 ±0.10	16.89 ± 0.1	15.90 ± 0.1	TNGN,TNGD
782.4	296			22.85 ±0.30	21.30± 0.20	20.30 ± 0.10				LT
790.4	304						18.85 ± 0.10	17.20 ±0.05	15.82 ±0.05	TNGN

[a]JD −245 4000.00.
[b]Phase is in days after the explosion epoch JD 245 4486 ± 4.

camera used by M. Mobberly peak, respectively, in the *V* and *R* bands. Therefore, although strictly these cameras were unfiltered, we nevertheless list the magnitudes obtained in the *V* or *R* columns of Table 5.

3.2 Near Infrared data

The NIR photometry was obtained with the Telescopio Nazionale Galileo (TNG) with Near-Infrared Camera Spectrometer (NICS) and with the AZT 24 telescope with SWIRCAM, in the *JHK* filters (Table 4). The NIR images were reduced using standard IRAF routines, with the jittered exposures first median-combined to obtain sky images in each band. Jittered images were then sky-subtracted, registered and finally combined. The instrumental magnitudes were measured on the combined images with SNOOPY package. Photometric calibration was carried out via relative Two Micron All Sky Survey (2MASS) photometry of the same local sequence stars used for optical data. The NIR magnitudes of SN 2008S are listed in Table 5.

3.3 Photometric evolution and bolometric light curve

In Fig. 3 (top panel), the *UBVRIJHK* light curves of SN 2008S are illustrated. These are characterized by a broad peak and a subsequent slow decline. In the *R* and *V* bands, there is clearly a fast rise to peak shown by early observations from a range of amateur telescopes. The peak occurs progressively earlier from the blue to the red bands (Table 6). The absolute magnitudes at maximum (Table 6), calculated adopting $\mu = 28.78 \pm 0.08$ mag and correcting for Galactic ($A_V = 1.13$ mag) and internal extinction ($A_V = 1$ mag), reveal that SN 2008S is brighter by 1–1.5 mag than the NGC 300 OT2008-1 and M85 OT2006-1 transients with which it has been compared (see Section 7.3).

The *BVRI* light curves show very similar temporal evolutions with three phases characterized by a different decline rate: a broad peak (about two weeks), a phase of steeper decline (γ_1 in Table 7) starting about 60 d after explosion, more pronounced at shorter wavelengths, and a flattening (γ_2) after 140 d, more evident at longer wavelengths. Due to the faintness of SN 2008S we do not have *U*- and *B*-band observations at the late phases to obtain an accurate estimate of the decline rate. In the NIR bands, the decline

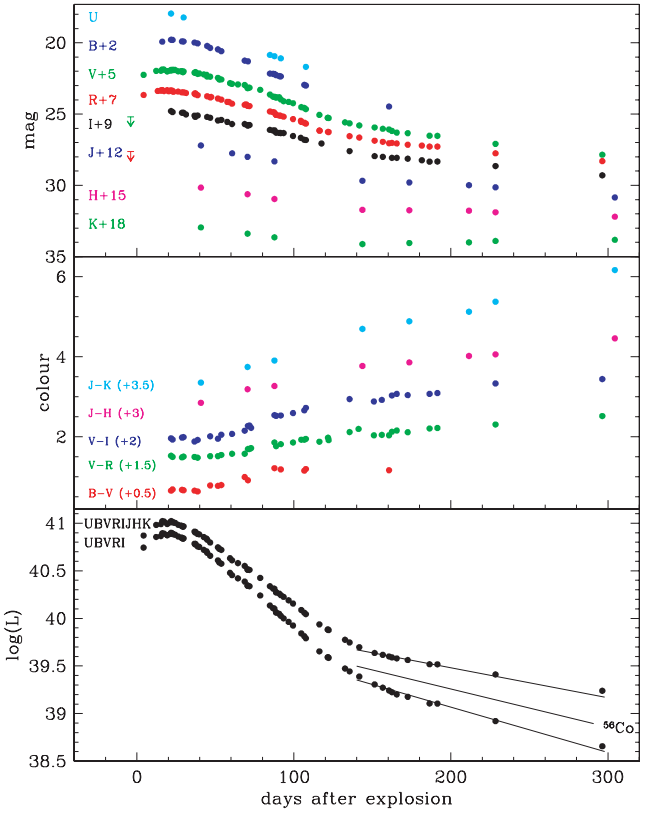

Figure 3. Top panel: *UBVRIJHK* light curves of SN 2008S. Middle panel: evolution of the $B-V, V-R, V-I, J-H, J-K$ colours. The magnitudes have been corrected for the adopted extinction according to the Cardelli extinction law. Bottom panel: the *UBVRIJHK* and *UBVRI* quasi-bolometric light curves. The ^{56}Co decay slope and the slope of *UBVRIJHK* and *UBVRI* curves are shown. Phase is in days after the explosion epoch (JD 245 4486).

rates are very slow until 120 d and show further a flattening (or a slight increase in *K* band) after this epoch.

The time evolution of the $B-V$, $V-R, V-I, J-H$ and $J-K$ colours of SN 2008S is shown in Fig. 3. All optical colours become progressively redder until about 200 d after the explosion. Subsequently the colours do not show significant evolution. This

Table 6. Epochs, apparent and absolute magnitudes of light curve maximum in the *BVRI* bands.

Filter	JD[a]	Ph[b]	m_{max}	M_{max}
B	509 ± 2	23	17.83 ± 0.05	−13.76 ± 0.16
V	505 ± 2	19	16.95 ± 0.05	−13.97 ± 0.16
R	503 ± 2	17	16.33 ± 0.05	−14.17 ± 0.16
I	502 ± 3	16	15.85 ± 0.05	−14.20 ± 0.16

[a]JD − 245 4000.00.
[b]Phase is in days after the explosion epoch JD 245 4486 ± 4.

Table 7. Decline rates in the *BVRIJHK* bands.

Filter	Ph_1[a]	γ_1(mag/100 d)	Ph_2[a]	γ_2 (mag/100 d)
B	50–100	4.5 ± 0.10	100–160	2.8 ± 0.10
V	50–120	4.0 ± 0.05	140–300	1.3 ± 0.06
R	60–120	3.4 ± 0.05	140–300	1.0 ± 0.05
I	60–120	2.8 ± 0.05	140–300	0.9 ± 0.06
J	40–120	2.4 ± 0.10	140–310	0.7 ± 0.05
H	40–120	1.5 ± 0.10	140–310	0.4 ± 0.10
K	40–120	1.5 ± 0.09	140–310	−0.2 ± 0.06

[a]Phase is in days after the explosion epoch JD 245 4486 ± 4.

trend is most evident for the $V - I$ colour. The NIR colours show a different evolution after about 200 d after the explosion: $J - H$ is slightly increasing while $J - K$ is steepening.

A 'bolometric' light curve (Fig. 3, bottom panel) was obtained by first converting *UBVRIJHK* magnitudes into monochromatic fluxes per unit wavelength, then correcting these fluxes for the adopted extinction ($A_V = 2.13$ mag) according to the extinction law from Cardelli, Clayton & Mathis (1989), and finally integrating the resulting SED over wavelength, assuming zero flux at the integration limits (the blue end of the *U* band and the red edge of the *K* band). We estimated the flux only for the phases in which *V*-band observations were available. The photometric data in the other bands were estimated at these phases by interpolating magnitudes in subsequent nights.

During the period 140–290 d, the *UBVRIJHK* 'bolometric' light-curve tail shows a decay rate of 0.88 ± 0.05 mag/100 d, very similar to that of ^{56}Co (1.023 mag/100 d from Huo et al. 1987), while the *UBVRI* 'bolometric' light curve is slightly steeper (1.3 ± 0.05 mag/100 d). Assuming that radioactive material was powering the late time photometric evolution of SN 2008S, we tried to estimate the ^{56}Ni mass synthesized by SN 2008S by comparing its *UBVRIJHK* quasi-bolometric light curve with that of SN 1987A from 140 to 300 d after explosion and assuming similar γ-ray deposition fraction:

$$M(^{56}Ni)_{08S} = M(^{56}Ni)_{87A} \times \frac{L_{08S}}{L_{87A}}, \quad (1)$$

where $M(^{56}Ni)_{87A}$ is the mass of ^{56}Ni produced by SN 1987A, L_{08S} is the luminosity of SN 2008S and L_{87A} is the luminosity of SN 1987A (at a similar epoch), also obtained from *UBVRIJHK* data. We adopt $M(^{56}Ni)_{87A} = 0.073 \pm 0.012\ M_\odot$ which is the weighted mean of values given by Arnett & Fu (1989) and by Bouchet, Danziger & Lucy (1991). For SN 2008S, we obtain an $M(^{56}Ni)$ of $0.0014 \pm 0.0003\ M_\odot$ where the error includes the uncertainties both in the assumed distance of SN 2008S and in the ^{56}Ni mass of SN 1987A. If we considered only optical data for both SN 2008S and SN 1987A we would obtain an $M(^{56}Ni)$ of $0.0011 \pm 0.0002\ M_\odot$. We estimated the ^{56}Ni mass also using the method of Hamuy (2003) assuming that all the γ-rays resulting from the decay of ^{56}Co into ^{56}Fe are fully thermalized:

$$M(^{56}Ni)_{08S} = 7.866 \times 10^{-44} L \exp\left[\frac{(t - t_0)/(1 + z) - \tau_{Ni}}{\tau_{Co}}\right] M_\odot, \quad (2)$$

where t_0 is the explosion epoch, $\tau_{Ni} = 8.76$ d the lifetime of ^{56}Ni and $\tau_{Co} = 111.26$ d is the lifetime of ^{56}Co. Using this method, we estimated $M(^{56}Ni)$ for each point of the radioactive tail and the average of these estimates gives an ejected ^{56}Ni mass of $\sim 0.0012\ M_\odot$. We remark that the estimated value of ^{56}Ni mass has to be considered as an upper limit if the ejecta—CSM interaction or an IR echo contributes to the tail of the bolometric light curve.

3.4 Data at other wavelengths

SN 2008S was serendipitously observed with *Spitzer* on 2008 February 6.8 UT during scheduled observations of the nearby SN 2002hh showing a strong MIR emission (Wesson et al. 2008). Images were obtained with Infrared Array Camera (IRAC) (3.6 μm, 4.5 μm, 5.8 μm and 8.0 μm) on day 17.3 and Multiband Imaging Photometer (MIPS) (24 μm) on day 18.0, uniquely early epochs for coverage of this wavelength region. The *Swift* satellite also observed SN 2008S in the optical, UV and X-ray bands on February 4.8, 6.0 and 10.5 UT, and detected it only in the optical images (Smith et al. 2009). SN 2008S was not detected on February 10.62 UT at radio frequencies with the Very Large Array by Chandra & Soderberg (2008). The contribution to the overall energy budget of SN 2008S at about 20 d after the explosion seems to be negligible at UV wavelengths but it is considerable at MIR wavelengths. In Section 4.1, we shall demonstrate that the large MIR luminosity must have been caused by an IR echo from pre-existing circumstellar dust.

4 SPECTRAL ENERGY DISTRIBUTION EVOLUTION

4.1 Up to day 120

The SED evolution of SN 2008S is shown in Fig. 4. During the first ∼120 d, the optical–NIR fluxes can be well reproduced by a single hot blackbody. The blackbody temperatures, radii and luminosities for some epochs are shown in Table 8 and plotted in Fig. 5.

The temperature fell monotonically from ∼8300 to ∼5000 K during this time. The radius declined slowly from about 1.9×10^{14} to 1.3×10^{14} cm, suggesting that the blackbody surface was defined by the photosphere through which the ejecta flowed.

Remarkably, a strong MIR excess was observed at ∼ 18 d after explosion by Wesson et al. (2008). The SED obtained with the *Spitzer* data was fitted by a 500 K blackbody modified by a dust emissivity that is inversely proportional to the wavelength, giving a luminosity of $21 \times 10^6\ L_\odot$. We have re-measured the *Spitzer* images, using the post-basic calibrated data (PBCD) products provided by the *Spitzer* pipeline. The 8 and 24 μm images showed strong irregular background at or near the location of the SN. We therefore subtracted serendipitously obtained pre-explosion 'templates' from the post-explosion images before proceeding with our flux measurements. The IRAC templates were taken from *Spitzer* programme 30292 (P.I. Meikle) and the MIPS template from programme 0230 (P.I. Barlow). The image matching and subtraction were performed as implemented in the ISIS v2.2 image-subtraction package (Alard 2000), and modified in a manner analogous to that described in Meikle et al. (2006). Aperture photometry was performed on the background-subtracted IRAC and MIPS images using the STARLINK

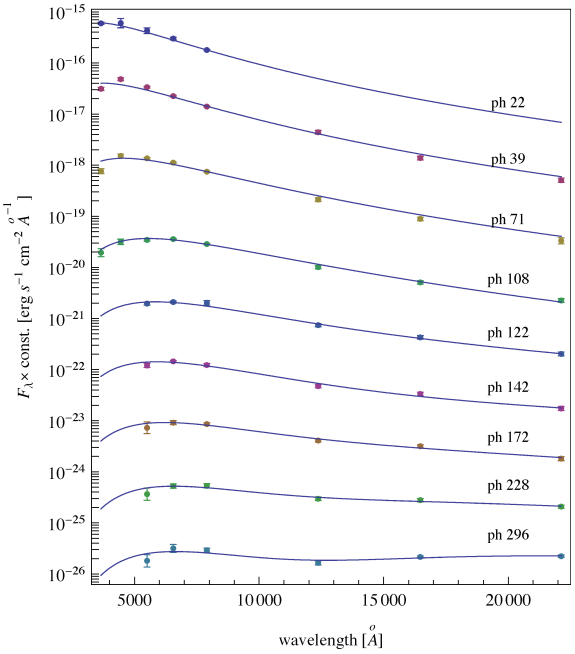

Figure 4. Temporal evolution of the observed SED of SN 2008S. Lines show the blackbody fits to the SED. Observed fluxes are corrected for the adopted extinction ($A_V = 2.13$ mag) according to the extinction law from Cardelli et al. (1989). Phase is in days after the explosion epoch (JD 245 4486).

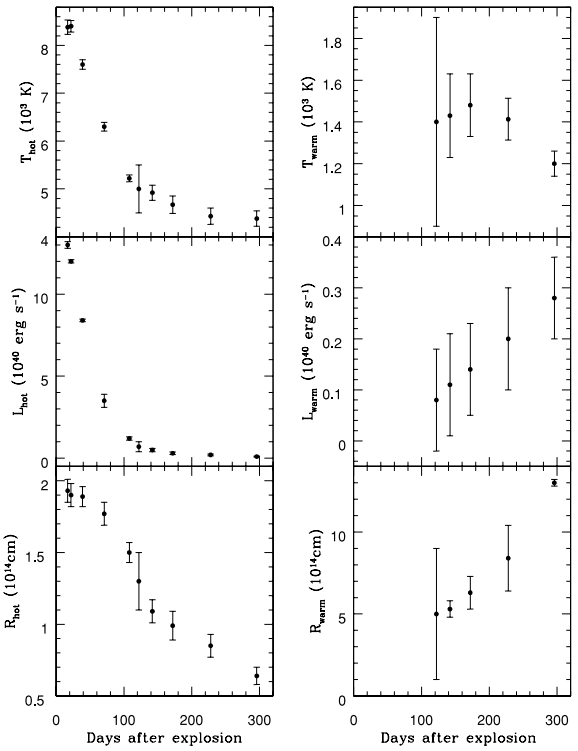

Figure 5. Temporal evolution of the parameters of the hot (left-hand panel) and warm (right-hand panel) blackbodies fitting the SED of SN 2008S. Phase is in days after the explosion epoch (JD 245 4486).

package GAIA (Draper 2000). A circular aperture of radius 5 arcsec was used for the photometry. This was chosen as a compromise between minimizing the effects of the residual irregular background emission at the SN location and minimising the size of aperture correction needed in the final flux determination. The aperture radius corresponds to a distance of ∼140 pc at SN 2008S. Residual background in the template-subtracted IRAC and MIPS images was measured and subtracted by using a clipped mean sky estimator, and a concentric sky annulus having inner and outer radii of 1.5 and 2 times the aperture radius, respectively. Aperture corrections were derived from the IRAC and MIPS point response function frames available from the Spitzer Science Center, and ranged from ×1.04 at 3.6 μm to × 2.12 at 24 μm. For IRAC, the aperture was centred by centroiding on the SN image. For MIPS, the aperture was centred visually on the SN, checking against the WCS coordinates. We found fluxes of 1.60 ± 0.02 mJy at 3.6 μm, 1.97 ± 0.03 mJy at 4.5 μm, 3.06 ± 0.07 mJy at 5.8 μm and 4.15 ± 0.05 mJy at 8 μm. The errors are statistical only and do not include calibration uncertainties which may amount to an additional ∼ ±5 per cent. The image subtraction at 24 μm left a substantial residual. We therefore also carried out aperture photometry on the unsubtracted 24 μm image. Consistent results were obtained for the subtraction and non-subtraction procedures. The mean flux derived from the two methods is 0.7 ± 0.1 mJy. Our IRAC and MIPS fluxes are consistent with those reported by Wesson et al. (2008). However, their errors are at least several times larger.

To investigate the nature of the MIR source, we carried out a simultaneous fit of two blackbodies to the SED at 17.3 d, and this is shown in Fig. 6. It can be seen that the blackbodies provide a plausible representation of the data. The hot blackbody has a temperature of 8076 ± 150 K and a radius of (2.1 ± 0.1) × 10^{14} cm,

Table 8. Parameters for a single blackbody fit (until 108 d after explosion) and for a two-component (hot and warm blackbodies) fit to the *UBVRIJHK* fluxes of SN 2008S.

Ph[a]	T_{hot} (K)	R_{hot} (10^{14} cm)	L_{hot} (10^{40} erg s^{-1})	T_{warm} (K)	R_{warm} (10^{14} cm)	L_{warm} (10^{40} erg s^{-1})	L_{warm}/L_{tot} (per cent)
17	8380 ± 150	1.93 ± 0.08	13 ± 0.2				
22	8400 ± 120	1.90 ± 0.08	12 ± 0.1				
39	7600 ± 100	1.89 ± 0.07	8.4 ± 0.1				
71	6300 ± 90	1.77 ± 0.08	3.5 ± 0.4				
108	5220 ± 70	1.50 ± 0.07	1.2 ± 0.1				
122	5000 ± 500	1.30 ± 0.20	0.7 ± 0.3	1400 ± 500	5.0 ± 4.0	0.08 ± 0.1	10
142	4920 ± 160	1.09 ± 0.08	0.5 ± 0.1	1430 ± 200	5.3 ± 0.5	0.11 ± 0.1	25
172	4670 ± 180	0.99 ± 0.10	0.3 ± 0.08	1480 ± 150	6.3 ± 1.0	0.14 ± 0.09	32
228	4430 ± 170	0.85 ± 0.08	0.2 ± 0.05	1413 ± 100	8.4 ± 2.0	0.20 ± 0.1	50
296	4380 ± 160	0.64 ± 0.06	0.1 ± 0.03	1200 ± 60	13 ± 0.2	0.28 ± 0.08	74

[a]Phase is in days after the explosion epoch JD 245 4486 ± 4.

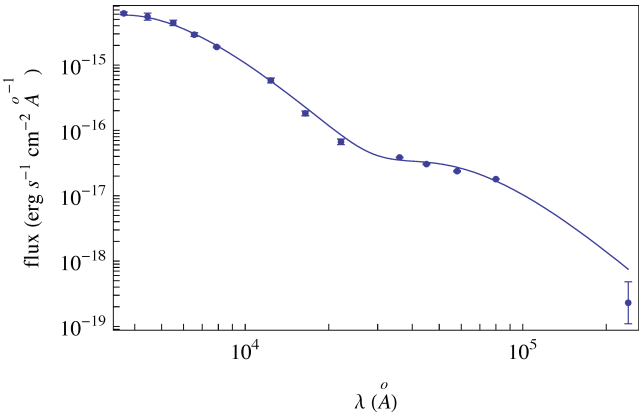

Figure 6. Fit of two blackbodies to the SN 2008S SED from optical to MIR at 17.3 d after explosion. The NIR data are obtained extrapolating data from phase 41. Observed fluxes are corrected for the adopted extinction (A_V = 2.13 mag) according to the extinction law from Cardelli et al. (1989).

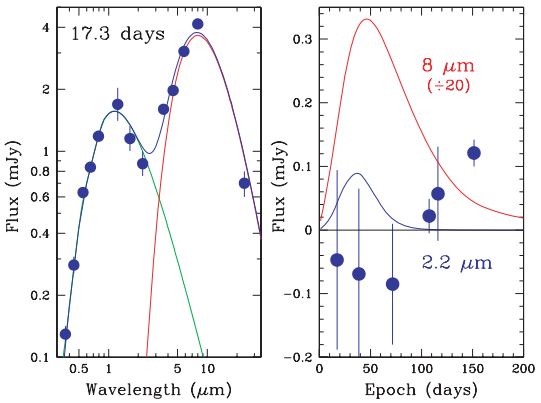

Figure 7. The left-hand panel shows the day 17.3 hot blackbody spectrum (green), the IR echo spectrum (red) and the combined spectrum (blue). These are compared with the day 17.3 optical–NIR points and the day 17.3 MIR points. The hot blackbody has a temperature of 8076 ± 150 K and a radius of $(2.1 \pm 0.1) \times 10^{14}$ cm, reddened using the extinction law of Cardelli et al. (1989) with $A_V = 2.13$ mag. The total optical depth through the CSM in the optical region is about 0.20, or $A_V = 0.22$ mag. The reddening effects of the CSM dust are included in the model. Consequently, the final IR echo model was reddened with $A_V = 2.13$–$0.22 = 1.91$ mag. For the IR echo model, a single-grain size was used with radius $a = 0.5$ μm. The grain material is amorphous carbon where, for wavelengths longer than $2\pi/a$, the grain absorptivity/emissivity is proportional to $\lambda^{-1.15}$ (Rouleau & Martin 1991). For shorter wavelengths, an absorptivity/emissivity of unity was used. The material density is 1.85 g cm^{-3} (Rouleau & Martin 1991). The CSM extended from 3×10^{16} cm to 3×10^{17} cm, with the dust density declining as r^{-2} (steady wind). The dust mass is 1.4×10^{-3} M$_\odot$. The right-hand panel shows the residual fluxes at 2.2 μm (blue points) at a number of epochs together with the 2.2 μm light curve from the IR echo model (blue). For the first five points, it can be seen that the model flux never exceeds the residual by much more than 1σ. The latest three residual points show the gradual emergence of the NIR excess (see text). Also shown is the IR echo light curve at 8 μm (red).

corresponding to an expansion velocity of 1430 km s^{-1}. These estimates are consistent with emission from the hot photosphere. The warm blackbody has a temperature of 585 ± 5 K. This temperature together with the reasonable match to the blackbody leads us to propose that the MIR emission must be due to warm dust. The radius of the warm blackbody is $(9.9 \pm 0.4) \times 10^{15}$ cm. For the SN to produce a surface of this radius in just 17.3 d would take a velocity of 66 200 ± 2700 km s^{-1}. Such an enormous velocity immediately rules out newly formed ejecta dust as the source of the MIR emission. The high velocity also rules out collision of the fastest moving ejecta with a dusty CSM. The only viable alternative appears to be an IR echo from CSM dust. To explore this possibility, we have matched an IR echo model to the MIR SED. Details of the model are given in Meikle et al. (2006). This assumes a spherically symmetric cloud of carbon grains centred on the SN, with a concentric dust-free cavity at the centre. For simplicity, a single-grain radius, a, is adopted. For ease of computation, we assumed that the grain material was amorphous carbon where, for wavelengths longer than $2\pi a$, the grain absorptivity/emissivity can be well-approximated as being proportional to $\lambda^{-1.15}$ (Rouleau & Martin 1991). For shorter wavelengths, an absorptivity/emissivity of unity was used. The material density is 1.85 g cm^{-3} (Rouleau & Martin 1991). Free parameters are the grain size, grain number density, the CSM radial density law, the CSM extent and the size of the concentric dust-free cavity. The outer limit of the CSM was set at 10 times that of the cavity radius, although this parameter is not critical. The input luminosity is a parametrized description of the *UBVRIJHK* 'bolometric' light curve (Fig. 3). Given the apparently low temperature of the dust, it is reasonable to assume that the IR echo made only a small contribution to the NIR flux implying a negligible overestimate of the bolometric light curve.

It was found that a range of parameters were able plausibly to reproduce the MIR flux. Matches were found for grain radii of 0.001–0.5 μm. The corresponding cavity range was 1×10^{17} cm to 3×10^{16} cm and the dust mass range was 10^{-2} to 10^{-3} M$_\odot$. Such masses of dust are entirely plausible within the CSM of a red (super)giant. For a typical wind velocity of 20 km s^{-1} and a dust-gas mass ratio of 0.01, the CSM dust masses we require in the IR echo model would be produced by a mass-loss rate of a few times 10^{-5} M$_\odot$ yr^{-1}. All the progenitor circumstellar dust within a particular radius would have been evaporated in the SN explosion. Given the peak luminosity of the SN, the evaporation radius for carbon grains is 3.5×10^{15} cm. Silicate grains would allow an evaporation cavity several times larger. However, there is little sign of an excess in the 8 μm band which we would expect from optically thin silicate grains. Nevertheless, even to account for a cavity radius of 3×10^{16} cm we must invoke some sort of episodic mass-loss history. The echo model spectrum is shown in Fig. 7 (left-hand panel). Also, shown are the hot blackbody spectrum obtained in the two-blackbody fits described above, and the combined hot blackbody and IR echo spectrum. This is compared with the optical–NIR–MIR observations at this epoch. The earliest NIR data were obtained at 40 d and so the 17.3 d fluxes were estimated by extrapolation of the NIR light curves. The extrapolation was performed by assuming constant $V - J, V - H, V - K$ colours during the first month. (If, instead, we assume a linear evolution of these colours, then the fluxes in the NIR bands would be smaller by 6 per cent, 22 per cent and 27 per cent in J, H, K, respectively.) The hot blackbody was reddened using the extinction law of Cardelli et al. (1989) with $A_V = 2.13$ mag. The total optical depth in the optical region through the CSM in the IR echo model is about 0.20, or $A_V = 0.22$ mag. The reddening effects of the CSM dust are included in the model. Consequently, the final IR echo model was reddened with $A_V = 2.13$-$0.22 = 1.91$ mag. Inspection of Fig. 7 shows that a satisfactory match to the data is obtained.

While the echo model easily reproduced the MIR flux, it also produced a certain level of NIR emission, with K being the brightest of the observed NIR bands. This, therefore, provides an additional

constraint on the echo model, i.e. the model has to be consistent with the NIR flux and its evolution. As explained above, satisfactory fits to the early-time optical–NIR SEDs were obtained using a single blackbody. There was little evidence of an NIR excess up to around 120 d. However, the blackbody fits are subject to error. We therefore investigated whether or not the predicted *K*-band fluxes of the echo model could be consistent with the uncertainties in the observed values and in the hot blackbody fit. For a number of epochs (17.3, 38.7, 71.7, 107.6, 116.2 and 151.4 d) we compared the echo model with the residual *K*-band fluxes derived by subtracting the hot blackbody flux to the observed one. The first five epochs were all consistent with a zero residual, but with uncertainties of $\sim \pm 0.1$ mJy. We then selected the echo model which yielded the smallest *K*-band fluxes and still produced a satisfactory match to the MIR fluxes. This was achieved with a 0.5 μm grain radius and a dust-free cavity of 3×10^{16} cm. The dust mass is $1.4 \times 10^{-3}\,\mathrm{M}_{\odot}$. The right-hand panel of Fig. 7 shows the residual fluxes at 2.2 μm together with the 2.2 μm light curve from the echo model (coloured blue). The error bars on the residual points were derived as a combination of the uncertainty in the observed/extrapolated points and the uncertainties in the hot blackbody fits. It can be seen that the model flux never exceeds the residual by much more than 1σ. The marginal negative shift of the first three residual points may be due to slightly imperfect blackbody fits such as might be caused by the actual extinction law being different from the one adopted. We deduce that it is quite plausible that the *K*-band flux from an IR echo would have been undetected, hence accounting for the near-zero residuals. The later three residual points show the gradual emergence of the NIR excess, discussed below. We conclude that the IR echo model accounts for the MIR flux as well as being consistent with all the shorter wavelength fluxes.

Also shown in Fig. 7 (right-hand panel) is the 8 μm light curve predicted by the IR echo model. We note that neither the 2.2 μm nor 8 μm light curves exhibit the flat top or plateau characteristic of the IR echo phenomenon. This is because, owing to the exceptionally low bolometric luminosity of SN 2008S, the radius of the dust-free cavity had to be small in order to attain a sufficiently high dust temperature. Indeed, the radius of the cavity in the model illustrated here is only 12 light days (3×10^{16} cm). Consequently, the decline of the light curves is actually dominated by the characteristic decline time-scale of the input bolometric light curve, which is about 70 d per e-fold, together with the r^{-2} dust density decline.

The final MIR observation of SN 2008S was at about 180 d, but at the time of writing, the data are not yet out of embargo (due 2009 August). Nevertheless, we can use the IR echo model to predict the fluxes at this epoch. We find that the 8 μm flux at 180 d is 1.3 mJy for the model discussed above, rising to around 5 mJy for models having a grain radius ~ 0.01 μm. Thus, the observed 180 day MIR fluxes should provide constraints for the grain size.

4.2 After day 120: dust formation?

To fit the SED at later epochs, we need the sum of a hot and a warm blackbody. We find statistical evidence for the emergence of a warm component as early as 120 d, viz. $\Delta\mathrm{BIC} = \mathrm{BIC}_{\mathrm{hot}} - \mathrm{BIC}_{\mathrm{hot+warm}} \simeq 1.5$. This becomes stronger with time, reaching $\Delta\mathrm{BIC} \simeq 5.7$ by 135 d. The hot component was still dominant at 172 d but by 296 d it contributed only 26 per cent of the total luminosity. The temperature of the warm component stayed roughly constant at 1400–1500 K until at least 228 d, but by 296 d had cooled to 1200 K. The luminosity and the radius monotonically increased during the 122–296 d period (Fig. 5).

A clear NIR excess was also observed at late phases in several other SNe (1997ab, 1979C, 1980K, 1982E, 1982L, 1982R, 1985L, 1993J, 1994Y, 1995N, 1998S, 2005ip, 2006jc) (e.g. Gerardy et al. 2002). The simplest explanation for the IR excess in both SN 2008S and these other SNe is thermal emission from warm dust heated by the SN. However, different locations, origins and heating mechanisms are possible. Specifically, IR excesses may be due to (a) newly formed dust in the ejecta, heated by radioactive decay or a reverse shock, (b) newly formed dust in a cool dense shell (CDS) formed by the SN shock/CSM collision and heated directly by the shock, by absorption of X-rays from the interaction region or by the bolometric light curve of the SN (a type of IR echo), (c) ejecta collision with pre-existing circumstellar dust or (d) an IR echo from pre-existing circumstellar dust heated by the SN bolometric light curve. These scenarios do not necessarily exclude one another. For example, in the case of SN 2006jc, the NIR excess was explained by Mattila et al. (2008) as a combination of IR echoes from newly formed CDS dust and from pre-existing dust in the CSM.

In the case of SN 2008S, we can immediately rule out an IR echo, whether from CDS or CSM dust, as being the cause of the late-time NIR excess. The bolometric light curve is too weak by a factor of $\sim$100 to account for the high dust temperatures and luminosities seen during the 200–300 d period. Moreover, for an IR echo scenario we would expect the phase and rise-time of the echo flux to be determined by the temporal behaviour of the bolometric light curve, which is about 35 d per e-fold beginning at 0 days (cf. Fig. 7, right-hand panel). Yet, the NIR excess does not appear until at least 120 d and has a characteristic rise-time of about 100 d.

This leaves dust heated by radioactivity or by energy from shock interaction with CSM. We first estimated the mass of such dust required to reproduce the NIR flux. We employed the escape probability model described in Meikle et al. (2007). Setting the expansion velocity of the dust cloud at $1000 \pm 50\,\mathrm{km\,s^{-1}}$, we found that for silicate dust grains in the ejecta the NIR excess was reproduced with a dust mass rising monotonically from about $0.2 \times 10^{-5}\,\mathrm{M}_{\odot}$ on day 122 to $1.2 \times 10^{-5}\,\mathrm{M}_{\odot}$ on day 296. During this time, the dust temperature fell from about 1300 to 1100 K, and the optical depth to the centre at 2.2 μm rose from 0.2 to 0.4. Thus, optically thin dust lying well within the velocity limit of refractory elements (say up to $\sim$2000 km s^{-1}) was able to reproduce the NIR excess. It follows that the derived masses indicate the minimum dust mass required. Reducing the size of the dust cloud caused it to quickly become optically thick, with the blackbody limit being approached at a radius corresponding to about $500\,\mathrm{km\,s^{-1}}$. Clearly, in this optically thick case the NIR observations do not restrict the mass of dust that could be concealed in the ejecta. If instead of ejecta dust, we assume the dust lay in the cloud which gave rise to the early time MIR echo, and was heated by ejecta collision, then the mass of dust required to reproduce the NIR flux remains much the same, but the optical depth falls to around 0.001. Finally, for optically thin dust, replacing silicate grains with amorphous carbon grains reduces the derived dust mass by a factor of about 10, due to the higher emissivity of carbon in the NIR region.

We conclude that a very modest mass of optically thin dust can account for the NIR excess flux. Moreover, it appears that the dust mass involved grew quite rapidly between 122 and 296 d. This dust may have condensed in the ejecta, heated by radioactive decay or a reverse shock. Alternatively, its location may have been much farther out in the CSM. To account for the early-time MIR flux, we had to invoke a 'dust-free cavity' of radius at least 3×10^{16} cm, with a dust mass beyond this limit of at least $10^{-3}\,\mathrm{M}_{\odot}$. However, to account for the later NIR excess flux, we have shown that the

required dust mass would be barely 1 per cent of this. Thus, it is quite feasible that sufficient dust to account for the NIR flux lay within the MIR echo cavity, with an inner limit fixed only by a dust evaporation radius which could be as small as $\sim 3 \times 10^{15}$ cm (see above). For the ejecta to reach this distance in, say, 150 d, would take a velocity of just 2300 km s^{-1}. The apparently increasing mass of dust might have been due to dust newly forming within a CDS. Alternatively, it simply may be that the shock swept up an increasing mass of pre-existing CSM dust.

Is it plausible that the NIR excess was due to new, radioactively heated ejecta dust? We have already shown that this can be achieved with a small mass of optically thin dust lying comfortably within the limits of refractory elements. However, the examination of the energy budget reveals problems. In Section 7.4, we estimate that SN 2008S produced only about 0.02 times of the mass of ^{56}Ni that was released by SN 1987A. If we scale the radioactive energy deposition law for SN 1987A (Li, McCray & Sunyaev 1993) to SN 2008S, we find that the deposited radioactive energy exceeded that of the dust luminosity by 8 times on day 122 falling to 1.25 times by day 228, i.e. there was sufficient radioactive energy to power the dust luminosity up to about day 228. However, by day 296, even if we assume the entire radioactive luminosity was deposited in the ejecta, it could only supply half of the dust luminosity, i.e. for radioactivity to account for the warm component flux at 296 days we would have to double the derived mass of ^{56}Ni. Another possible difficulty is that, even if we focus on just the period 122–228 days, the fraction of radioactive energy deposited in the dust increases from ∼12 per cent to ∼80 per cent and yet the average number density of ejecta dust stayed approximately constant. Why then did the dust-deposition fraction show such a large increase? It may be related to the detailed distribution of the grain growth and radioactive material. But, given the day 296 energy deficit, perhaps a more plausible explanation is that at least part of the NIR excess had another cause. This might be the reverse-shock heating of new ejecta dust. Alternatively, it might be IR radiation from shock-heated newly formed CDS dust or pre-existing circumstellar grains. We conclude that, while the earlier NIR excess could have been entirely due to new, radioactively heated dust in the ejecta, as time went by, an increasing proportion of the flux must have been powered by other mechanisms.

NIR/MIR-based evidence for newly formed dust in the ejecta or CDS of SNe has been reported in the cases of SN 1987A (Moseley et al. 1989; Suntzeff & Bouchet 1990; Meikle et al. 1993; Roche, Aitken & Smith 1993), SN 1998S (Pozzo et al. 2004), SN 2004gd (Sugerman et al. 2006; Meikle et al. 2007), SN 2004et (Kotak, Meikle & Farrah 2009) and SN 2006jc (Smith, Foley & Filippenko 2008; Di Carlo et al. 2008; Mattila et al. 2008). Dust masses of typically 10^{-4} to 10^{-3} M$_\odot$ are directly observed, although larger masses may exist in optically thick clumps. Dust condensation in the ejecta or in a CDS can be also be demonstrated via the effects of the dust on optical radiation. In particular, it can attenuate the red wings of spectral lines, causing an apparent blue shift of the line profiles (Danziger et al. 1991; Lucy et al. 1991; Elmhamdi et al. 2003; Pozzo et al. 2004). However, the spectra of SN 2008S are of insufficient resolution or wavelength precision to enable us to make this test.

5 SPECTROSCOPIC DATA REDUCTION AND ANALYSIS

We spectroscopically monitored SN 2008S for eight months with several telescopes, and details of the spectroscopic observations are reported in Table 9. Spectra were reduced (trimmed, overscan and bias-corrected, flat-fielded) using standard routines within IRAF. An optimal variance weighted extraction of the spectra was carried out using the IRAF routine APALL. Wavelength calibration was performed using the spectra of comparison lamps acquired with the same instrumental configuration as the SN observation. Flux calibration was done using spectrophotometric standard stars observed with the same instrumental setup. Approximate spectral resolutions were estimated from the full-width-at-half-maximum (FWHM) of the night sky lines. The wavelength calibration is accurate to ±1 Å for ISIS spectra, ±2 Å for DOLORES and DBSP spectra and ±3 Å for CAFOS, ALFOSC and AFOSC spectra. Atmospheric extinction corrections were applied using tabulated extinction coefficients for each telescope site. The spectra of standard stars have also been used to identify telluric features and to remove these from the SN spectra. Spectra of similar quality obtained during the same night were combined to increase the S/N. To check the flux calibration, *BVRI* magnitudes were estimated by integrating the spectra convolved with standard filter functions using the task CALCPHOT within the IRAF package STSDAS. The spectro-photometric magnitudes were compared to the photometric observations and, whenever necessary, a scale factor was applied to match the photometric observations. The flux calibration is accurate to within approximately 10 per cent.

5.1 Line identification

We identified Hα, Hβ, Hδ, [Ca II] doublet ($\lambda\lambda$7292,7324) and Ca II triplet ($\lambda\lambda\lambda$8498,8542,8662), Fe II (multiplets 27, 28, 37, 38, 40, 42, 46, 48, 49, 72, 73, 74, 92, 186, 199), [O I] and Mn II (multiplet 4) in emission and Na I doublet ($\lambda\lambda$5890,5896) in absorption in early spectra (Fig. 8 and Table A2). In the more recent spectra O I (multiplet 4, λ8446) and Na I D are visible in emission, while the O I triplet in absorption seems to disappear. These emission lines are likely produced in different regions with different ionization states and velocities. The low ionization is likely due to high column density material with high optical depth.

5.2 Spectroscopic evolution

The spectra of SN 2008S do not show significant evolution during the temporal interval from 15 days to 8 months after the explosion (Fig. 10), the continuum becoming progressively redder and fainter with time. All spectra consist of a nearly featureless continuum with superimposed strong Balmer emission lines, [Ca II] doublet and Ca II NIR triplet. The most remarkable change in the latest spectra is the presence of Na I D and O I (λ8446) in emission. We do not detect high-velocity absorption lines at any phase, suggesting that the ejecta are not directly visible. The lines do not show a P-Cygni profile typical of an SN explosion at very early phase but exhibit two different kinds of profiles. [Ca II] and Fe II lines show only a narrow asymmetric component with a red wing (Fig. 10). The Hα, Hβ and Ca II NIR triplet lines show evidence for a multicomponent profile (Fig. 9, top and middle panels). We focused our analysis on Hα, the [Ca II] doublet and the Ca II triplet since they are the most prominent lines and visible in all spectra estimating line parameters with the IRAF task SPLOT. The velocities are FWHM and those of Hα and Ca II (λ8662) have been measured by deblending the multiple-component profile and assuming a Gaussian profile for each component. To measure the peak position at different phases, we selected the spectra acquired with a slit width smaller than the seeing, hence considering only spectra with accurate wavelength calibrations.

Table 9. Journal of spectroscopic observations of SN 2008S.

JD[a]	Ph[b]	Telescope	Grism or grating	Range (Å)	Resolution (FWHM) Å	Exp. time (s)
500.8	15	WHT	R1200R	6200–6880	0.7	1800
501.3	16	NOT	Gr 4	3600–8700	19	800
504.3	19	WHT	R158R	5500–10000	10	800
507.7	22	TNGD	LR-R	5150–10225	11	1800
513.7	28	CAO	Gr 4	3900–7800	24	3600
514.8	29	WHT	R1200R	7025–7560	0.8	900
514.8	29	WHT	R300B	3170–5350	3.5	900
523.7	38	CAHAT	G-200	4950–10260	13	2700
529.8	44	INT	R300V	3750–9340	5	1000
532.7	47	CAHAT	G-200	4950–9750	14	3000
539.8	54	TNGD	VHR-V	4650–6600	5	2400
552.8	67	CAO	Gr 4	3790–7790	24	3600
553.7	68	CAHAT	r-100	5800–9600	9	3600
557.8	72	CAO	Gr 4	3500–8450	24	3600
561.7	76	TNGD	VHR-R	7110–7560	4.1	2700
582.6	97	CAHAT	r-200	6178–10600	11	3600
588.7	103	CAHAT	b-200	3900–8850	11	1700
606.7	121	WHT	R316	5520–8260	6	2700
609.7	124	WHT	R316	7190–10400	4.7	1800
667.7	182	WHT	R158	5400–9900	10	2700
668.7	183	WHT	R158	5400–10200	6	2700
741.7	256	HP200	300	3300–5600	8	1800
741.7	256	HP200	158	5800–10300	11	1800

[a]JD − 245 4000.00.
[b]Phase in days with respect to the explosion date JD 245 4486 ± 4.
WHT = the 4.2 m William Herschel Telescope (WHT) with the Intermediate dispersion Spectrograph and Imaging System (ISIS); NOT = the NOT with ALFOSC; TNGD = the TNG with DOLORES; CAO = the Copernico telescope with AFOSC; CAHAT = the 2.2 m telescope at CAHA with CAFOS; INT = the 2.5 m Isaac Newton Telescope (INT) with the Intermediate Dispersion Spectrograph (IDS); HP200 = the 5.08 m Hale Telescope with the Double Spectrograph Specs (DBSP) at Palomar Observatory.

Hydrogen. The intensity of Hα decreases by a factor of approximately 10 from the earliest spectrum to the latest (Table 10). It follows the flux in *R* band (see Fig. 11) during the first 60 days, and then shows a flattening (the *R*-band light curve changes the decline slope shortly after). The Hα profile in the first high-resolution ISIS spectrum exhibits three different kinetic components as shown in Fig. 10. The narrow, intermediate and broad components correspond to velocity widths (FWHM) of $v_{\rm n} \sim 250\,{\rm km\,s^{-1}}$, $v_{\rm i} \sim 1000\,{\rm km\,s^{-1}}$ and $v_{\rm b} \sim 3000\,{\rm km\,s^{-1}}$, respectively, in this early spectrum. The Hα intensity and the broad component velocity width, $v_{\rm b}$, show a similar temporal behaviour, decreasing quickly until about 60 d after explosion and more slowly after this epoch (Fig. 11 and Table 11). The intermediate component velocity width, $v_{\rm i}$, shows a less abrupt decline. The narrow component, $v_{\rm n}$, is not resolved in several spectra at intermediate phases but appears to stay constant until 60 days after the explosion and is not visible after this epoch (Fig. 11 and Table 11). This component of Hα seems also to be asymmetric, but the resolution of our spectra is not adequate to analyse its profile in detail.

The Hα profile could be interpreted as broad underlying emission due to the ejecta, an intermediate component resulting by shocked material behind the interaction front between ejecta and CSM and a narrow component from unshocked CSM. However, the lack of any high-velocity absorption component, or P-Cygni profile, is a fairly strong argument that the broad emission is not a direct measurement of the ejecta velocities. This profile may be also interpreted as a narrow core with broad wings resulting from multiple scattering events with thermal electrons, an escape mechanism for line photons favoured by the small photospheric velocity observed for SN 2008S at all phases (Dessart et al. 2009). The electron scattering in a dense (Thomson optical depth of ∼3–4) CS shell lying beyond the SN photosphere was suggested by Chugai (2001) as an explanation for the very broad wings of Hα in SN 1998S. We compare the Hα profiles of SN 1998S and SN 2008S in Fig. 12. The redshift in the Hα peak decreases after about 100 d (Fig. 13), although the uncertainties in the wavelength calibration mean that this shift has only a modest significance. The EW(Hα) increases with time, becoming very large at late phases (about 900 Å). There are two processes proposed for the origin of H emission lines: photoionization with subsequent emission by recombination or collisional excitation (Drake & Ulrich 1980). The first cannot explain the increase of the EW(Hα) with time, so collisional excitation of Hα from the $n = 2$ level seems to be the more likely mechanism to explain Balmer emission, especially at the latest phases. In the first spectra, Hβ shows a multicomponent profile similar to Hα (Fig. 9), but this feature is too weak to analyse its profile in detail. The Hα/Hβ ratio is larger than the recombination value of about 3 and increased from 4 at 15 d to 10 at 256 d after the explosion. This ratio depends critically on several parameters: electron density (N_e), electron temperature, external radiation field strength and optical depth in $\tau_{\rm H\alpha}$ (Drake & Ulrich 1980). The three most important processes which can change the line intensity with respect to the recombination value are: Balmer self-absorption (important at low density), collisional excitation and de-excitation (important at high density) (Drake & Ulrich 1980).

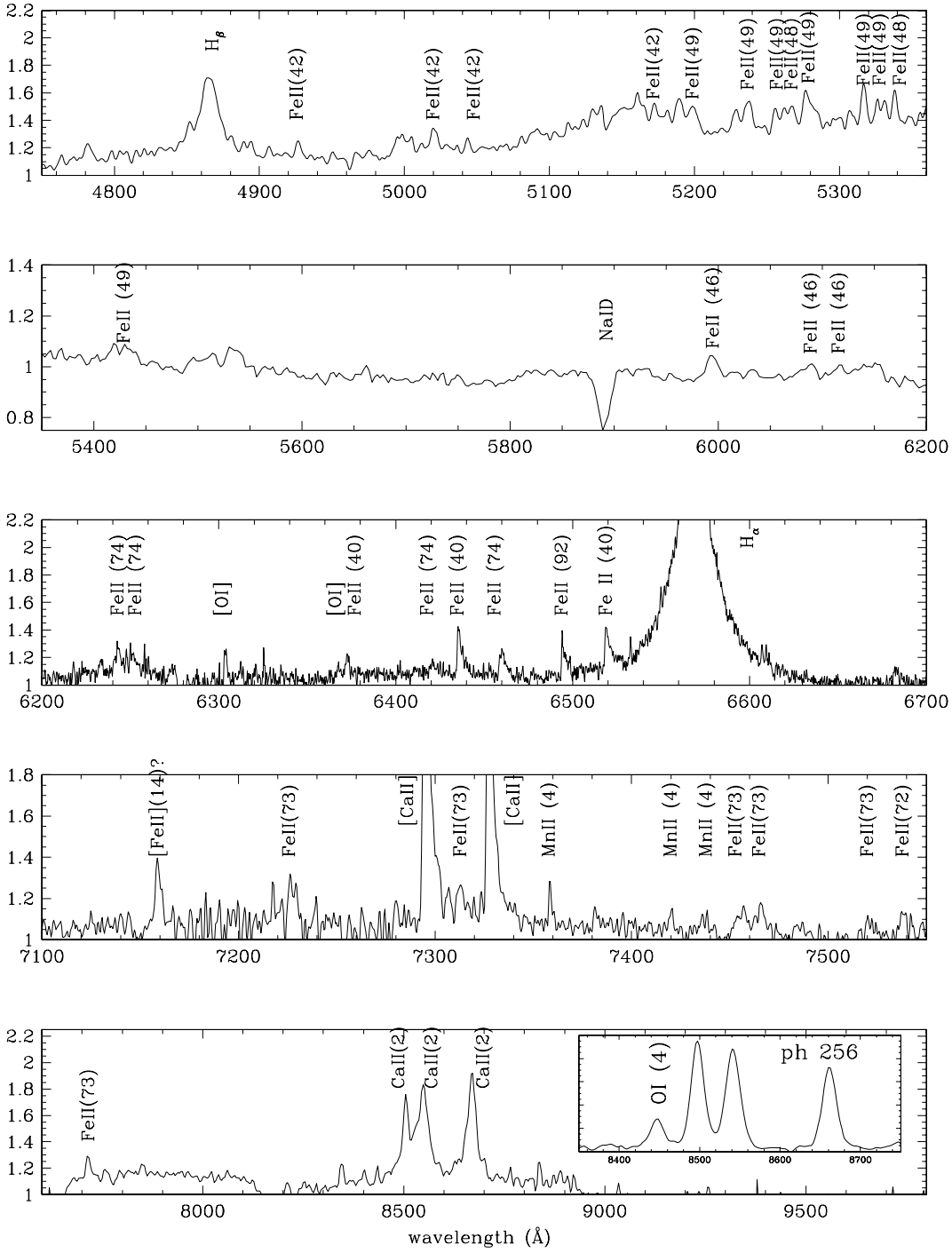

Figure 8. Spectral lines observed in SN 2008S spectra. From the top to the bottom panel: spectra obtained at WHT (phase 29), at TNG (phase 22), at WHT (phase 15), at WHT (phase 29), at WHT (phase 19). Inset: spectrum obtained with HP200 (phase 256). Phase is in days after the explosion epoch (JD 245 4486) and wavelength is in the observer frame.

Collisional excitation processes cause the Hα/Hβ intensity ratio to increase, and the N_e value at which these processes become important inversely depends on $\tau_{\mathrm{H}\alpha}$. At the first epochs, the Hα/Hβ intensity ratio indicates of $10^{10}\,\mathrm{cm}^{-3} \leq N_e \leq 10^{12}\,\mathrm{cm}^{-3}$ given the observed temperatures in SN 2008S (see Section 4) so the collisional processes may have an important role. The Balmer decrement, observed in SN 2008S, may be a sign of the high optical depth and the interaction with a high-density CSM. In particular, its evolution is likely led by the increase of $\tau_{\mathrm{H}\alpha}$ with time.

Calcium. The strength of the [Ca II] doublet decreases by a factor of ∼10 over 100 d and line ratio Hα/[Ca II] ranges from 9 to 18 over about 260 d (Table 10). We did not see any temporal evolution of the intensity ratio for the [Ca II] doublet (always around the value of 1 ± 0.2) and of the position of the peak. The [Ca II] doublet very likely originates in a lower density region with respect to the Ca IR triplet. As discussed by Chevalier & Fransson (1994), the [Ca II] doublet originates from radiative de-excitation from the metastable $3d^2$D level, which is highly populated. The probabilities for the two [Ca II]

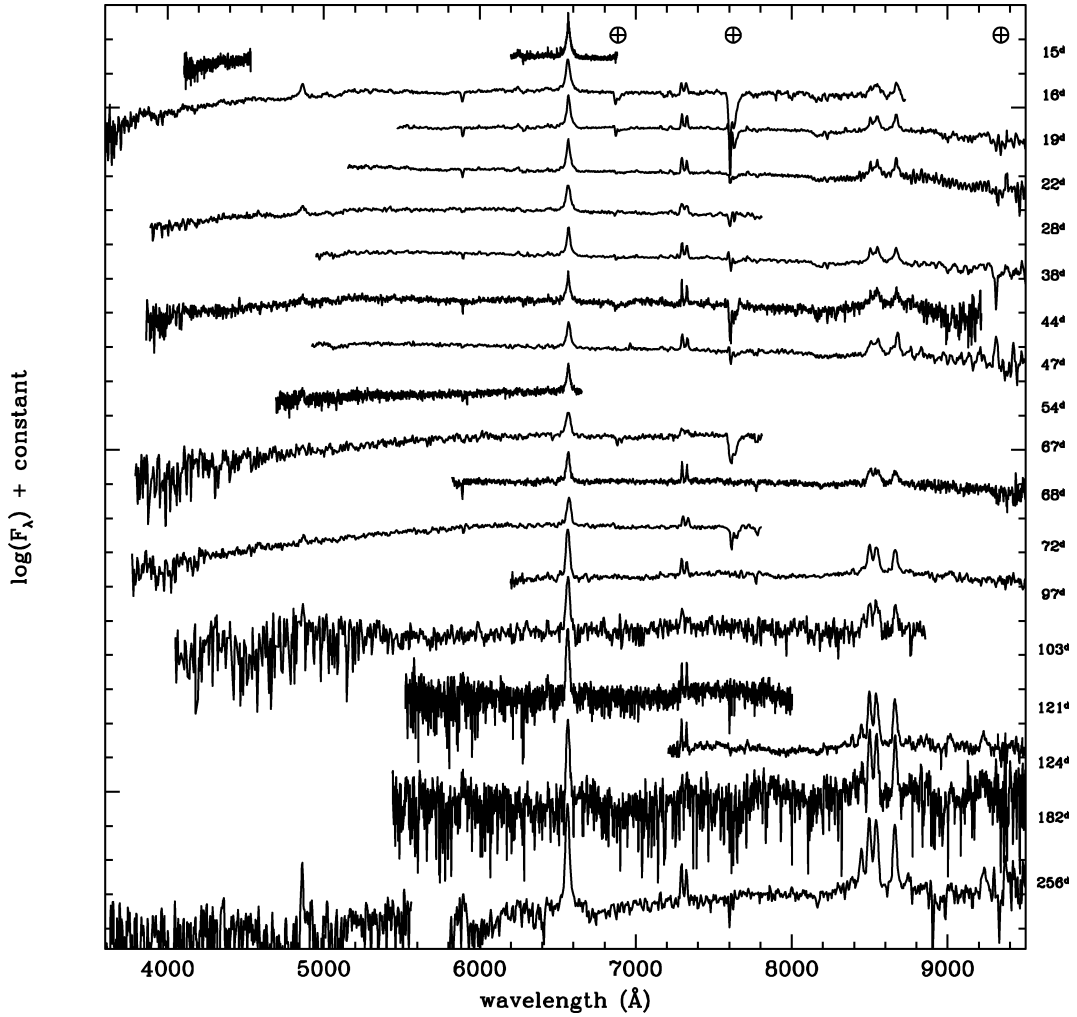

Figure 9. Time sequence of SN 2008S spectra. The spectra are corrected for Galactic extinction. The phase reported to the right of each spectrum is relative to the explosion epoch (JD 245 4486) and wavelength is in the observer frame. The ⊕ symbols mark the positions of the most important telluric absorptions.

transitions originating within the same multiplet are approximately equal and the threshold to ionize Ca^{+} to Ca^{++} from this metastable level is at 1218.8 Å. The gap between this threshold and the Lyα line is 3.2 Å corresponding to about 800 km s^{-1}. Only gas with higher velocity can ionize Ca II by absorbing Lyα photons suppressing [Ca II] emission. The presence of strong [Ca II] doublet in the first SN 2008S spectra may be indicative of little Ca II being ionized, and hence a narrow Lyα line. The [Ca II] doublet shows a velocity width (FWHM) of about 250 ± 60 km s^{-1} that is comparable to that of the narrow component of both Hα and Ca II triplet. This velocity width remains constant while the line profile shows an evolution: it is asymmetric during the first three months after the explosion and starts to be more symmetric after this epoch (Fig. 14). In Section 7.2, we propose an explanation for this behaviour based on a toroidal geometry in the CSM.

The Ca II NIR triplet must originate in a different region from that which produces the [Ca II] doublet since it shows both a multicomponent profile (Fig. 15) and a decreasing redshift with time (Fig. 16). Velocities for the different components are reported in Table 11 and are consistent with those of Hα. The intensity ratios of the infrared triplet to Hα and to [Ca II] increase with the time (Table 10). To investigate if the peak position of Hα, the [Ca II] doublet and the Ca II NIR triplet show any temporal evolution, we again exploited the BIC factor. We compare the BIC values obtained by fitting the spectral time series with either a position constant in time or a temporal evolution (parametrized as a straight line with a non-null slope), $\Delta\mathrm{BIC} = \mathrm{BIC}_{\mathrm{slope}} - \mathrm{BIC}_{\mathrm{const}}$. For H$\alpha$ there is only a marginal evidence for an evolution, $\Delta\mathrm{BIC} \simeq 0.3$. For the Ca II doublet, evolution is not favoured ($\Delta\mathrm{BIC} \simeq -1.0$ and -0.8 for the first and the second line, respectively). Finally, there is strong evidence for a decreasing redshift for the Ca II NIR triplet, $\Delta\mathrm{BIC} \simeq 13.9$.

Oxygen, Iron and Sodium. The [O I] (λ λ6300,6364) doublet is visible in the first high-resolution spectrum with a very low velocity width (FWHM), about 80 km s^{-1}. These are collisionally suppressed at high density, so likely originate in a slow-moving and low-density region. O I(λ8446) appears at the latest phases with a velocity width of about 530 km s^{-1} similar to those of the Hα and Ca II intermediate components at the same phase. The Fe II lines, visible in the first high-resolution spectrum, appear to have only a narrow component with velocity width around 200 km s^{-1} and the same profile as [Ca II]. The Na I D feature, visible in absorption in the early spectra, seems to show two blended lines: the Galactic contribution and the host galaxy doublet. In the spectra acquired at 182 and 256 d, this feature clearly appears in emission. This evolution is indicative of the circumstellar origin of the Na I D and is a clear sign of the high density of CSM. The evolution of EW(Na ID), illustrated in Section 2.3, may be due to an evolution of the

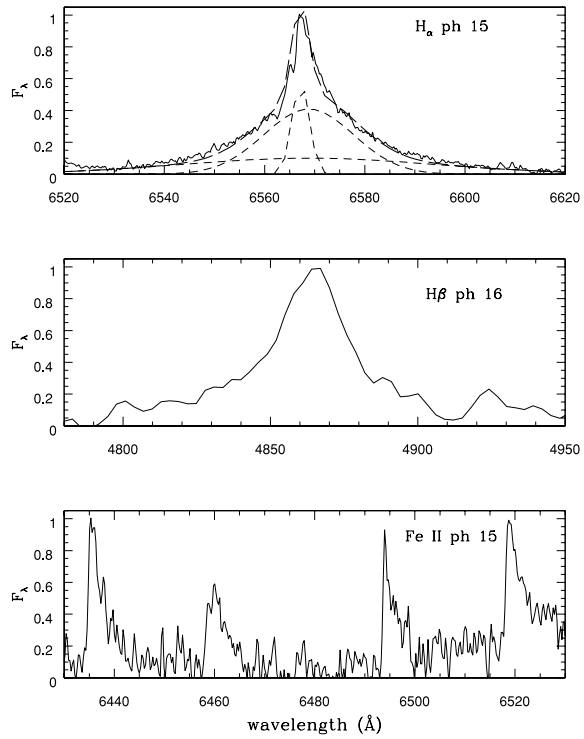

Figure 10. Line profiles at about two weeks after the explosion epoch (JD 245 4486): in the top panel, the multicomponent profile of Hα in the high-resolution ISIS spectrum (the three Gaussian components are shown as thin dotted lines and their combination is shown as thick dotted line); in the middle panel Hβ profile in the NOT spectrum; in the bottom panel the profiles of Fe II lines in the ISIS spectrum. Wavelength is in the observer frame. The flux densities have been normalized to the line peaks.

ionization conditions in the CSM and in the ejecta of SN 2008S since the EW is related to the ionization stage of Na I.

6 THE PROGENITOR OF SN 2008S

6.1 Optical and NIR pre-explosion images

We carried out an independent analysis on the deepest pre-explosion optical and NIR images that we could locate, similar to that presented in Prieto et al. (2008b). We added some further data and recalculated all the limits as some values in that paper were taken from heterogeneous references rather than original data. We used optical images from the Gemini North and Large Binocular Telescope and NIR images from the Bok 2.3 m telescope (Fig. 17, top panels). To ensure an accurate positioning of SN 2008S on all the pre-explosion images, we used an image of SN 2008S obtained with the Auxiliary Port Imager (AUX) on the WHT on 2008 February 08. The camera has a pixel scale of 0.11 arcsec pixel^{-1}, and a 1024 pixel TEK2 CCD. A single *R*-band image of 300 s was taken, and although it was at high airmass (2.47) the image quality was 1.03 arcsec. The position of SN 2008S was determined on all the pre-explosion images to an accuracy of 0.1 arcsec, and we confirm the results of Prieto et al. (2008b) that there is no optical or NIR counterpart detected. We calculated the 3σ detection limits for each of the optical images from the LBT and Gemini images and these are reported in Table 12.

The K'-band image was obtained from Knapen et al. (2003) with the Bok 2.3 m telescope of the Steward Observatory on 1999 October 17 with the PISCES camera, a HAWAII HgCdTe array of 1024 $\times$ 1024 pixels of 0.5 arcsec on the sky. The dithered exposures resulted in co-added total exposure time of between 1000 and 2000 s, depending on field location, and the image quality was 2.3 arcsec. The WHT AUX *R*-band image was used to locate the position of SN 2008S on the frame by matching the positions of 12 stars located within 1.7 arcmin of the SN in both *R* and *K* images. The geometric transformation resulted in an rms to the fit of 108 milliarcsec, and at this transformed position there is no detection of a source in the K'-band image. The zero-point for this frame was estimated using five 2MASS stars located close to the SN, and the calculated 3σ limiting magnitude was estimated to be $K = 18.0$ mag. The mean magnitudes of several of the faintest point sources visible in the vicinity of the SN was $K = 18.3 \pm 0.3$ mag. Hence, we adopt $K = 18$ mag as the sensitivity limit of this frame.

6.2 *Spitzer* MIR pre-explosion images

As discussed in Prieto et al. (2008b), several epochs of archival MIR imaging from the *Spitzer Space Telescope* are available. We analysed IRAC (3.6–8.0 μm) images (Fig. 17, bottom panels) with the longest integration times from programmes 3249, 20256 and 30292 (P.I. Meikle). Aperture photometry was carried out on the

Table 10. Evolution of the intensity of Hα, Ca II (λ8662) and [Ca II] doublet. Intensities are in units of 10^{-14} erg cm^{-2} s^{-1}.

JD[a]	Ph[b]	I (Hα)	I (Ca II λ8662)	I ([Ca II] λ7291)	I ([Ca II] λ7323)
501	15	3.7 ± 0.20	1.40 ± 0.08	0.42 ± 0.02	0.41 ± 0.02
505	19	3.5 ± 0.20	1.26 ± 0.07		
508	22	3.2 ± 0.15	1.18 ± 0.07		
514	28	2.7 ± 0.15			
524	38	2.1 ± 0.12	0.86 ± 0.06	0.37 ± 0.01	0.35 ± 0.01
530	44	1.6 ± 0.12			
540	54	1.3 ± 0.10			
554	68	1.2 ± 0.10			
562	76			0.17 ± 0.009	0.15 ± 0.009
583	97	1.1 ± 0.10	0.45 ± 0.05	0.12 ± 0.008	0.10 ± 0.009
589	103	0.98 ± 0.09			
607	121	0.65 ± 0.07	0.37 ± 0.04	0.051 ± 0.003	0.053 ± 0.004
742	256	0.39 ± 0.05	0.22 ± 0.03	0.022 ± 0.001	0.021 ± 0.001

[a]JD − 245 4000.00.
[b]Phase is in days with respect to the explosion date JD 245 4486 ± 4.

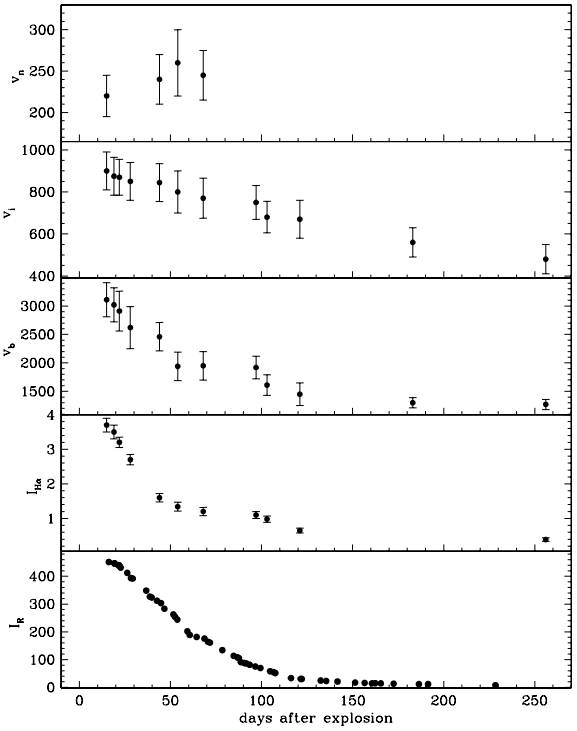

Figure 11. Temporal evolution of Hα kinematic components and intensity. From the top to the bottom panel: evolution of the velocity of the narrow (v_n), intermediate (v_i), broad (v_b) component, the integrated flux of Hα and the *R* band. Velocity widths (FWHM) are in km s^{-1} and integrated fluxes are in units of 10^{-14} erg cm^{-2} s^{-1}.

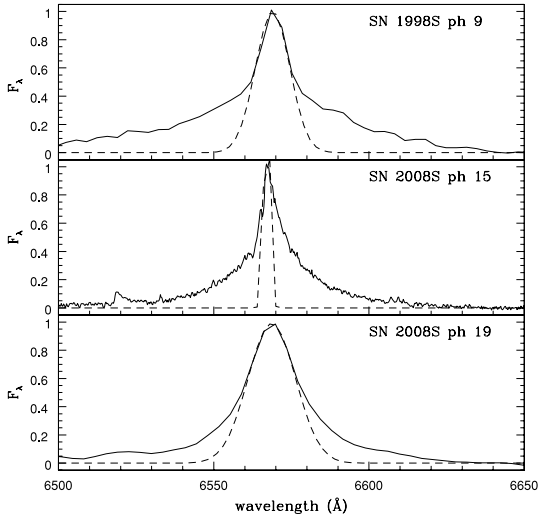

Figure 12. Comparison between Hα profiles in SN 1998S (phase 9 d) and SN 2008S at two different phases (15 and 19 d). Phase is in days after the explosion epoch (JD 245 0869 for SN 1998S and JD 245 4486 for SN 2008S). Wavelength is in the observer frame. A Gaussian profile that matches the line peak is shown as a dashed line.

post-BCD images using GAIA. A circular aperture of 2.0 arcsec was used. Aperture corrections were derived using the point response function frames available from the Spitzer Science Center. The residual background level was measured using a clipped-mean sky estimator, and a concentric sky annulus having inner and outer radii of 1.5 and 2 times the aperture radius, respectively. The resulting flux densities are listed in Table 12 and are consistent with the values reported in Prieto et al. (2008b). We used the AUX image of SN 2008S and the deep, wide field *Gemini i*-band image to determine the position of SN 2008S on the *Spitzer* 4.5, 5.8 and 8.0 μm images using differential astrometry. In each case, the uncertainty in the positioning of SN 2008S on the *Spitzer* images was 0.3 arcsec. This uncertainty is a combination in quadrature of the geometric transformation rms and the uncertainty in the measurement of the centroid of the progenitor object detected by Prieto et al. (2008b). The difference between SN 2008S and the progenitor object is 0.16 ± 0.30 and 0.14 ± 0.30 arcsec for the 5.8 and 8.0 μm images, respectively. However, there is a small difference in the position of the progenitor source in the 4.5 μm image. This is separated from the SN 2008S position by 0.51 ± 0.33 arcsec. On close inspection of the images, it appears that the source in the 4.5 μm image may well be extended compared to its 5.6 and 8.0 μm counterparts (see also fig. 1 in Prieto et al. 2008b). This might suggest that the 4.5 μm source is actually a blend of two or more sources. It seems fairly secure that SN 2008S is coincident with the 5.8 and 8.0 μm sources, and we have no evidence to suggest that they are extended or non-stellar. The suggestion that the

Table 11. Evolution of the three kinematic components (broad, v_b; intermediate, v_i; narrow, v_n) in Hα and Ca II (λ8662) features. The velocity widths (FWHM) are in km s^{-1}.

JD[a]	Ph[b]	v_b (Hα)	v_i (Hα)	v_n(Hα)	v_b (Ca II λ8662)	v_i(Ca II λ8662)	v_n (Ca II λ8662)
501	15	3110 ± 300	900 ± 90	220 ± 30			
504	19	3020 ± 300	875 ± 90		3000 ± 350	850 ± 90	264 ± 30
508	22	2910 ± 350	870 ± 85				
514	28	2620 ± 370	850 ± 90				
524	38				2280 ± 300	753 ± 60	
530	44	2460 ± 250	844 ± 90	240 ± 30			
540	54	1940 ± 200	790 ± 90	260 ± 40			
554	68	1950 ± 250	770 ± 95	245 ± 30			
583	97	1920 ± 200	750 ± 80		2040 ± 200	720 ± 80	
589	103	1610 ± 180	680 ± 75				
607	121	1450 ± 100	670 ± 90				
610	124				1340 ± 200	660 ± 70	
669	183	1300 ± 90	560 ± 70		1290 ± 200	550 ± 70	
742	256	1270 ± 100	480 ± 70		1260 ± 300	540 ± 80	

[a]JD − 245 4000.00.
[b]Phase is in days with respect to the explosion date JD 245 4486 ± 4.

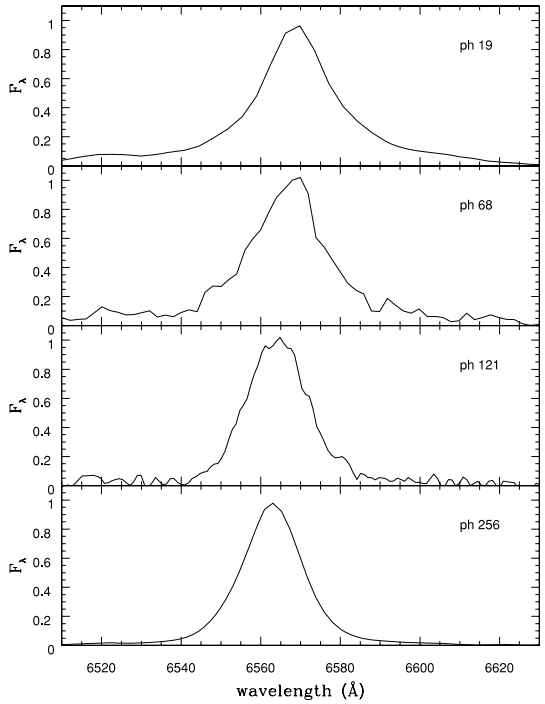

Figure 13. The peak position and profile of Hα at 19 d, about 2 months, 4 months and 9 months after the explosion epoch (JD 245 4486). Wavelength is in the observer frame. Flux density has been normalized to the line peak at each phase.

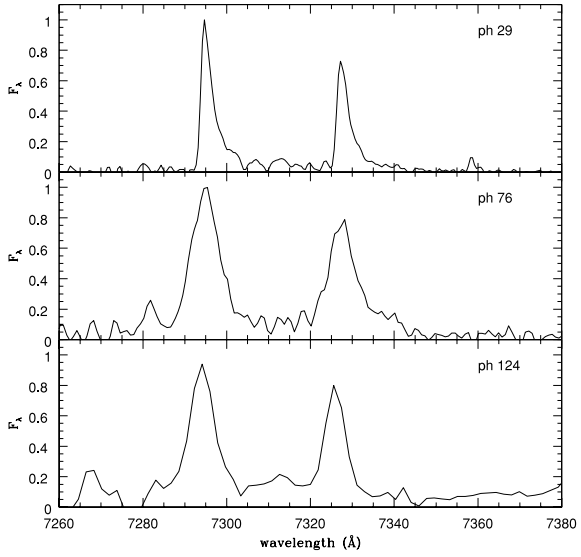

Figure 14. Profile of [Ca II] doublet at about 1 month, 3 months and 4 months after the explosion epoch (JD 245 4486). Wavelength is in the observer frame. Flux density has been normalized to the line peak at each phase.

4.5 μm source may be slightly extended could just be due to contamination from nearby, but unrelated flux at this wavelength. But the possibility remains that the source is a blend and this needs to be clarified with late, deep imaging with *Spitzer* and ground-based high-resolution studies.

Prieto et al. (2008b) also reported aperture photometry for the individual pre-explosion *Spitzer* epochs. They found no evidence for variability in the flux of the pre-explosion source over the

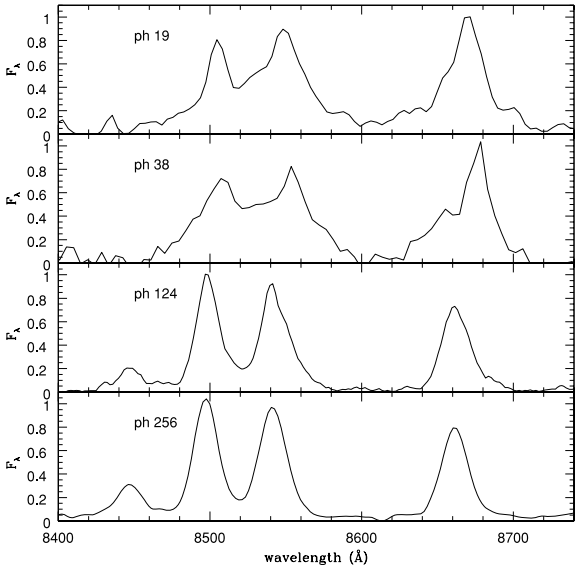

Figure 15. Profile of Ca II NIR triplet at about 20 d, 1 month, 3 months, 4 months and 9 months after the explosion epoch (JD 245 4486). Wavelength is in the observer frame. Flux density has been normalized to the line peak at each phase.

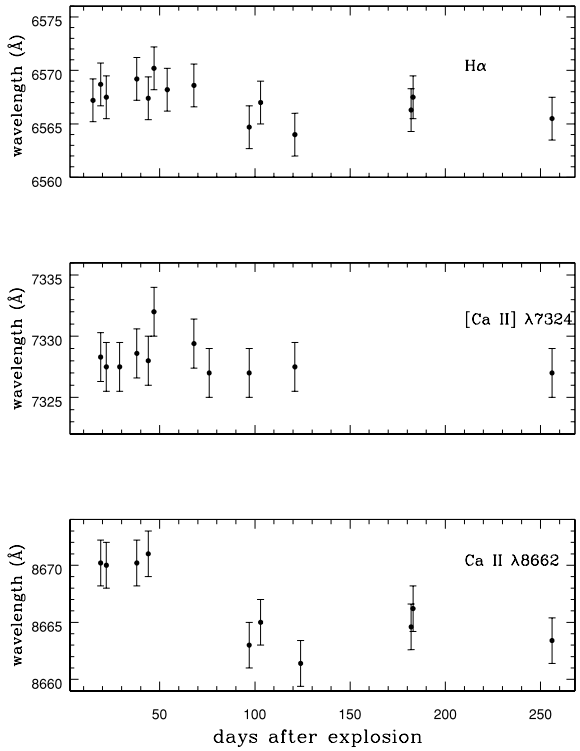

Figure 16. The peak position of Hα, [Ca II] (λ7324) and Ca II (λ8662) as a function of phase. Phase is in days after the explosion epoch (JD 245 4486) and wavelength is in the observer frame.

$\sim$1000 d covered. Our photometry is based on the combined *Spitzer* images. To detect possible variability on the source flux, we compared the post-BCD 4.5 μm images from 2004-11-25 and 2006-08-12 where the pre-explosion source was well detected. We first aligned the images using the centroid coordinates of 13 point-like sources around the pre-explosion source position. The aligned images were matched and subtracted using the ISIS 2.2 (Alard 2000)

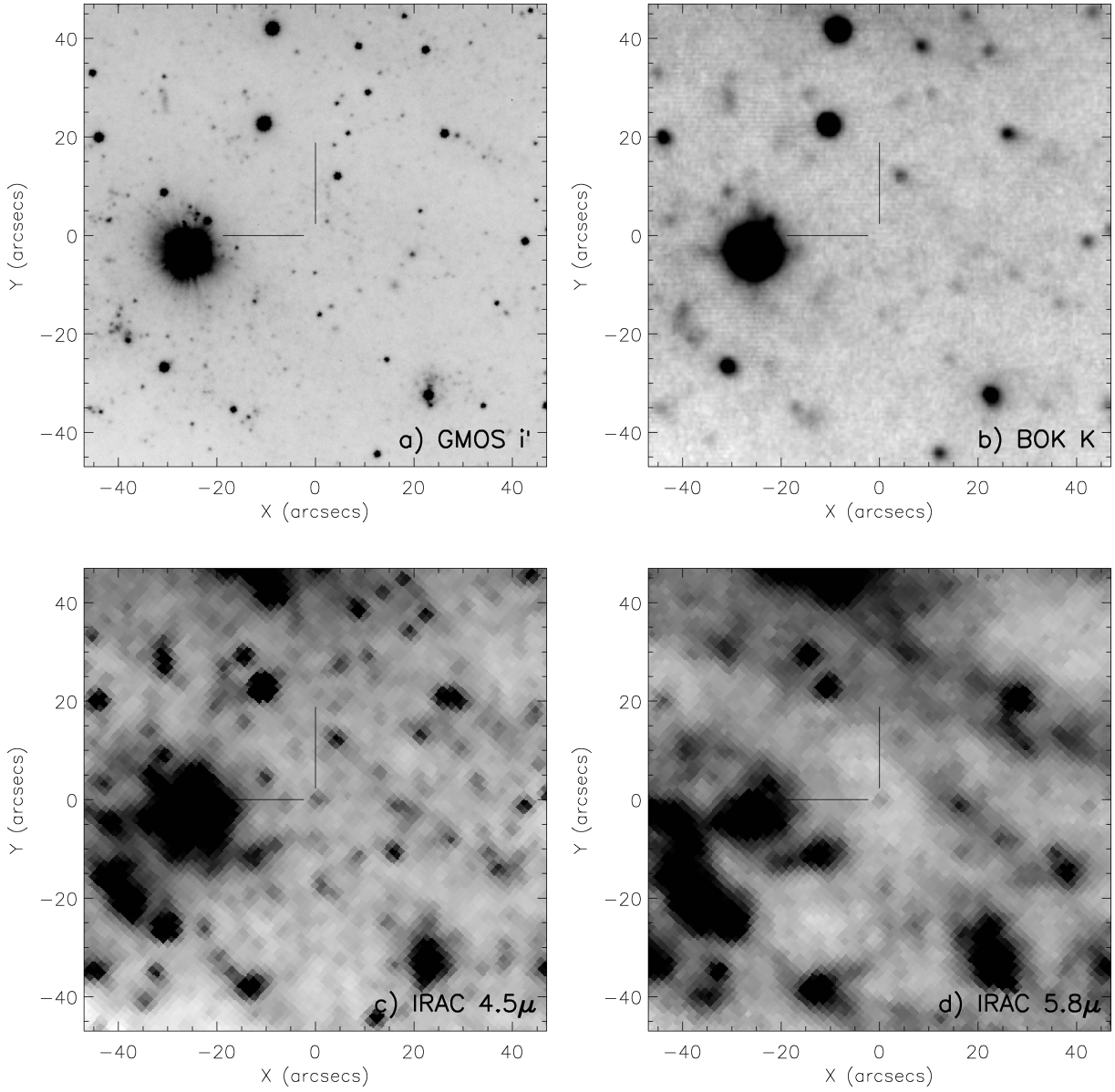

Figure 17. Pre-explosion images of SN 2008S. (a) The Gemini GMOS i'-band image showing no progenitor detection to deep limits. (b) K-band image from the Bok telescope, again showing no detection in the NIR. (c) and (d): *Spitzer* images at 4.5 and 5.8 μm, originally presented by Prieto et al. (2008b). We find some evidence that the 4.5 μm may be slightly extended. This can only be tested with higher spatial resolution images once the SN fades.

Table 12. Fluxes and magnitudes measured in the position of SN 2008S on pre-explosion images.

Waveband	Instrument	Flux or magnitude	Units
U	LBT	>25.1	Vega Mag
B	LBT	>24.5	Vega Mag
V	LBT	>24.5	Vega Mag
i	GMOS-N	>24.4	Vega mag
K'	PISCES	>18	Vega Mag
3.6 μm	IRAC	<3.6	μJy
4.5 μm	IRAC	21.3 ± 1.5	μJy
5.8 μm	IRAC	45.6 ± 2.4	μJy
8.0 μm	IRAC	59.5 ± 4.3	μJy

image-subtraction package (for details see also Meikle et al. 2006). No residual above the noise was apparent in the subtracted image at the pre-explosion source position. This confirms the findings of Prieto et al. (2008b) on the lack of variability of the pre-explosion source.

6.3 Analysis of the pre-explosion images

To determine whether the precursor object detected in the *Spitzer* images is a viable stellar progenitor, we modelled the MIR emission using the radiative transfer model DUSTY, in a manner similar to that applied to dusty RSG and asymptotic giant branch (AGB) stars in the (LMC) by van Loon et al. (2005a). In Fig. 18, we show two fits. In the first case (model *A*), we show a warm circumstellar, spherical, dust shell with $T_{\rm dust} = 800$ K (at the inner boundary), which has an optical depth of $\tau_V = 150$ ($\tau_{8\,\mu{\rm m}} \sim 2$). We assume

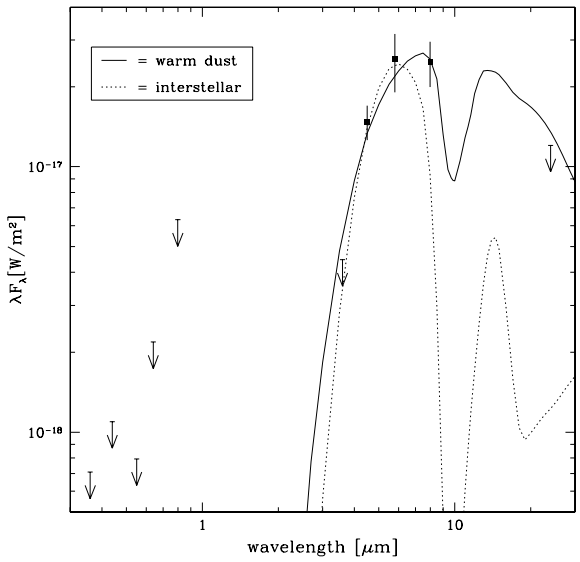

Figure 18. The MIR SED of the SN 2008S progenitor star and the two fits obtained using the radiative transfer model DUSTY. Model *A* (thin line) consists of a warm circumstellar, spherical, dust shell with $T_{\rm dust} = 800$ K (at the inner boundary), which has an optical depth of $\tau_V = 150$. Model *B* (dotted line) consists of a block of optically thick interstellar dust with $A_V = 140$ mag.

that the central exciting source is a blackbody of 3000 K (a cooler temperature does not make a major difference to the MIR output). The outer radius of the shell is 454 AU (2.2 milli-parsec), but its thickness needs to be $R_{\rm outer}/R_{\rm inner} < 5$ to fit the SED. The dust in this case consists of silicates with a typical grain size distribution. The inferred luminosity of the central star is $\log {\rm L/L}_\odot \simeq 4.6$ and with such a dense shell all of the stellar energy is absorbed by the dust and hence all appears as reprocessed MIR flux. While this may seem a plausible model and scenario for a dust shell around a massive, embedded star, the extinction toward the central star would be $A_V = 163$ mag. Hence, in this case of a spherical, dense (but radially thin) circumstellar shell the optical and K' bands offer no meaningful constraints on the stellar SED. Prieto et al. (2008b) suggested a thermally radiating sphere to account for the observed SED (with a blackbody temperature $T_{\rm dust} = 440$ K, $\log {\rm L/L}_\odot \simeq 4.5$ and $R_{\rm BB} = 150$ AU).

The second case (model *B*) shown in Fig. 18 is a block of optically thick interstellar dust with $A_V = 140$ mag. The extinction law from Cardelli et al. (1989) is used, although this does not fit particularly well around the 8 μm detection. The extremely high value of extinction would imply densities similar to those in the cores of molecular clouds, and the central stellar source would need to be $\log {\rm L/L}_\odot \simeq 6.9$ (again we have assumed a blackbody of 3000 K).

The main problem with either of the above two scenarios is that the extinction we see towards SN 2008S can be robustly estimated to be less than $A_V < 4$ mag and is more likely to be of the order of $A_V = 2.2$ mag. Hence, if a spherical dust shell surrounding an exciting source is the explanation for the precursor SED, then the explosion must have destroyed nearly all the dust within the 454 AU shell. Bode & Evans (1980), Wright (1980) and Dwek (1983) have suggested that the UV-optical luminosity from SNe could destroy dust within a spherical cavity around the progenitor star. Additionally, UV flashes have been recently observed from Type II-P SNe (Gezari et al. 2008; Schawinski et al. 2008). However, these calculations assume a small optical depth, and a more detailed estimate of an optically thick CSM which is evaporated by UV–optical photons within a γ-ray burst beam has been undertaken by Waxman & Draine (2000). They suggest that a GRB could clear very high column densities of dust (e.g. $A_V \sim 30$ mag) within several parsec of the explosion. Taking these calculations, scaling the destruction radius $R_{\rm d}$ by $\sqrt{\rm L}$ [where for an SN X-ray/UV flash we take $E \sim 10^{46}$ erg, as found in Gezari et al. (2008) and Schawinski et al. (2008)] and reducing the effective flux by the solid angle of the GRB beam in comparison to the isotropic SN energy, a destruction radius of a few milli-parsec is found. In the optically thick regime of Waxman & Draine (2000), the destruction radius does not depend strongly on the density, or A_V, with $R_{\rm d}$ changing by a factor of less than 2 when $n_{\rm H}$ changes by a factor of 10^5. Hence, it may be feasible for a dust embedded SN to clear a large enough cavity to become relatively unobscured, even at relatively high dust densities.

Prieto et al. (2008b) proposed that the properties of the precursor source are very similar to those of dust enshrouded RSG and AGB stars in the LMC as studied by van Loon et al. (2005a). All of the carbon stars in van Loon et al. (2005a) have $\log {\rm L/L}_\odot < 4.09$ which is somewhat too low to result in a CCSN. Smartt et al. (2009) show the lowest luminosity progenitors to be around 4.3 dex, and stellar evolutionary models would suggest progenitors of luminosity <4.1 dex would have initial masses of 5 $M_\odot$ or less. Hence, these C-type stars are not plausible counterparts to the SN 2008S progenitor and are not viable progenitors for a CCSN. More luminous and massive stars than these AGB objects (which are above the core-collapse threshold) tend to have less optically thick envelopes. For example, IRAS 04516−6902 is likely to have $A_V \sim 13$ mag but would be too faint to match the precursor of SN 2008S. In fact, all of the RSGs in LMC with luminosities above 4.3 dex would not be bright enough at 8 μm to account for the observed flux before the explosion of SN 2008S. In addition, many of them would be too bright in the *K* or *I* band to be consistent with our observed upper limits (although adjusting the extinction could help hide this shorter wavelength flux).

IRAS 05280−6910 (van Loon, Marshall & Zijlstra 2005b) is an extreme case where the star is hardly detectable in the optical and might appear an appealing source for comparison. However, in this case the 24 μm flux of IRAS 05280 − 6910 would be much brighter than the limit set for the pre-explosion source. Hence, we agree that the suggestion of Prieto et al. (2008b) of a dust-enshrouded RSG is initially very appealing, and the dust destruction even at such high column densities does not appear unrealistic. However, we cannot easily match SN 2008S progenitor quantitatively with any of the known dusty RSG or AGB stars in the LMC and Galactic samples, in full agreement across the optical and NIR non-detections. Our conclusions are consistent with the work of Thompson et al. (2008), who show that stars with the same MIR properties as the progenitor of SN 2008S are very rare in the nearby spiral M33. They find only ∼10 objects with similar magnitudes and colour which they associate with the high-luminosity tail of the AGB sequence. They conclude that this phase is a short period in the lives of a reasonable fraction of massive stars, perhaps linked to large mass ejections and subsequent dust formation episodes in the last ∼0.1 per cent of a stellar lifetime. The fact that these types of stars are not common in the LMC-studied populations supports this conclusion.

In Fig. 19, we show a Hertzsprung–Russell diagram (HRD) with the STARS model tracks of Eldridge & Tout (2004). The positions of Galactic RSGs are shown (from Levesque et al. 2005) along with the region in which RSG progenitors of recent nearby Type II-P SNe lie ($\log {\rm L/L}_\odot = 4.3^{+0.5}_{-0.3}$; Smartt et al. 2009). The luminosity of the progenitor has been estimated at $\log {\rm L/L}_\odot = 4.6 \pm 0.3$. Although

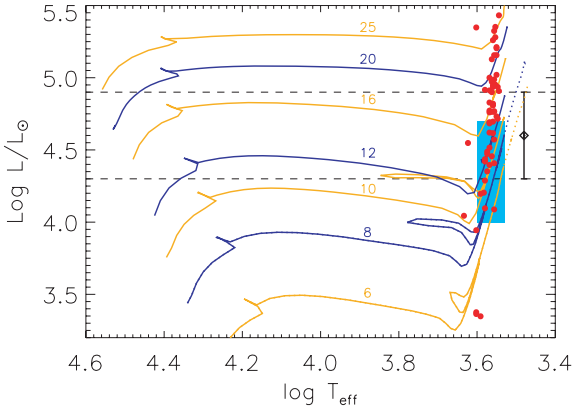

Figure 19. An HR diagram showing the positions of RSGs in the Galaxy from Levesque et al. (2005) (points) and the region (shaded region) in which red supergiant progenitors of normal II-P SNe have been seen (Smartt et al. 2009). The luminosity of the progenitor of SN 2008S is estimated as $\log L/L_{\odot} = 4.6 \pm 0.3$, and $T_{\rm eff} = 3000$ K is consistent with the SED (black point with error bar). However, the $T_{\rm eff}$ is unconstrained from the DUSTY model. The dotted lines limit the region of luminosities allowed for the progenitor. The tracks are the STARS models from Eldridge & Tout (2004).

we have estimated the temperature of the exciting source as $T_{\rm eff} = 3000$ K in the DUSTY model, this number is not well constrained, as a hotter star can be placed inside a denser, geometrically thinner envelope and produce a similar SED. The dotted lines at the extrema of the luminosity ranges show where the progenitor may lie. The tracks of 6–8 $M_{\odot}$ stars which have gone through second dredge-up are shown as dotted line. As discussed by Eldridge, Mattila & Smartt (2007), many different stellar evolutionary models predict that super-AGB stars (in the 6–9 $M_{\odot}$ range) that have gone through second dredge-up can rise to higher luminosities and lower effective temperatures than their higher mass counterparts. These stars may be thermally unstable, pulsating and prone to large mass ejection events. The luminosity of the SN 2008S progenitor star is, within the uncertainties of both the measurements and models, consistent with the position we would expect in the HRD for a 6–8 $M_{\odot}$, star which has gone through second dredge-up and has developed an O–Ne–Mg core within which electron-capture collapse could occur. The luminosity of the progenitor has been interpreted as an indication of a mass of 10–20 $M_{\odot}$ (Prieto et al. 2008b; Smith et al. 2009; Bond et al. 2009; Berger et al. 2009). However, as seen in Fig. 19, the luminosities of 6–8 $M_{\odot}$ progenitors after second dredge up are consistent with the bolometric luminosity of the progenitor of SN 2008S.

So far, our analysis has assumed that the pre-explosion MIR source is a single object and not, for example, an embedded cluster of stars within which the progenitor arose. One cannot definitively rule out the latter, and we noted above that there is some evidence to suggest that the 4.5 μm image is extended. However, we would argue that it is unlikely to be a cluster for two reasons. First, the total luminosity is not unusually high for a stellar source, and if it is a cluster that hosted an SN explosion then the progenitor is likely the dominant source of flux. Secondly, the cluster would still need to have an extinction similar to that found for the stellar source assumption and the dust would, presumably, be extended over a few parsec (typical cluster size). However, we estimated the likely destruction radius at only a few milli-parsec which seems too small to have an embedded object within a cluster clear the line of sight of intervening dust. The CS dust shell appears to be more plausible.

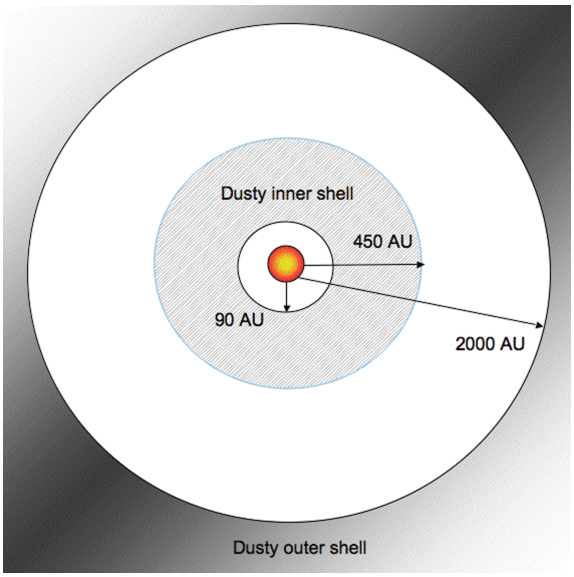

Figure 20. Schematic illustration of the pre-explosion geometry of SN 2008S.

7 THE NATURE OF SN 2008S

7.1 Pre-explosion CSM

Super-AGB stars lose mass at a high rate and their circumstellar medium have a high density and complex geometry. The circumstellar environment of SN 2008S suggests such a progenitor star. The progenitor analysis demonstrates the presence of a dusty optically thick shell around SN 2008S with an inner radius of nearly 90 AU, while the MIR echo analysis indicates a second, dusty outer shell of inner radius ∼2000 AU (Fig. 20). The two different shells imply that the progenitor star experienced a variation in the mass-loss rate. The physical size of the inner shell indicates that it was probably circumstellar and the result of mass loss due to a steady wind rather than eruptive ejection (see also Thompson et al. 2008). If we assume that the optical depth to the source scales as r^{-1} in a freely expanding wind, τ_V to the progenitor was about a factor of ∼10–20 larger before explosion, i.e. the inner shell was highly obscuring. The dust within this shell was probably evaporated in the explosion. In contrast, the much larger distance of the dust in the outer shell meant that it was not destroyed by the radiation from the SN photosphere. Instead, the enormous MIR flux observed at 17.3 d can be explained as an IR echo from the outer shell dust whose mass we estimate to be $\sim 10^{-3}$ $M_{\odot}$. We also propose that, if we invoke a toroidal geometry in the outer shell, then the asymmetric profile of the [Ca II] and Fe lines can also be explained. This is addressed below.

7.2 The photometric and spectroscopic evolution

SN 2008S exhibited a very slow photometric evolution and almost no spectral variability during the first 9 months, implying a long photo-diffusion time and a high-density CSM (Schlegel 1990). Nevertheless, photometric and spectroscopic observations suggest that there are three distinct phases: the maximum light phase (0–50 d after the explosion), the flattening of Hα intensity (60–100 d) and the NIR excess phase (from about 120 d).

During the first two phases, the SN 2008S optical–NIR SED can be fitted with a single blackbody with a radius of about

2×10^{14} cm. The blackbody temperature and radius declined monotonically, with the temperature falling from ∼8000 to 5000 K.

During the first phase, all the spectra showed prominent emission lines of Hα, the [Ca II] doublet, the Ca II NIR triplet, faint Fe II emission lines and Na I D in absorption. None of the H, Ca or Fe lines exhibits P-Cygni profiles, providing additional evidence of a high-density CSM. Some of the Na I D absorption probably has an origin in the CSM, given the observed high density and rapid evolution of the EW during the first month. The only forbidden lines visible in the early spectra are the intense [Ca II] and weak [O I] doublets, probably produced in the low-density inter-shell zone.

At about 60 d after the explosion, the decline of SN 2008S light curves steepened, while the Hα intensity remained constant until about 100 d. During this phase, the Hα narrow component disappeared and the [Ca II] profile lost its earlier asymmetry. We suggest, as an explanation of the change in the [Ca II] profile, that the progenitor CSM took the form of a toroid, viewed almost edge-on. At early times, obscuration of the [Ca II] emission zone by the outer shell dust would affect predominantly the fraction of the gas moving towards us, thus attenuating the blue wing. However, by 60 d, much of the ejecta would have reached the inner shell. (It would take a velocity of only ∼2500 km s^{-1}.) This would be expected to produce a strong burst of hard radiation arising from the ejecta-shell impact. This, in turn, might evaporate the outer shell dust resulting in the increasing symmetry of the [Ca II] line profiles. However, there are several difficulties with this scenario. (a) We surmise that the [O I] doublet formed in the same low-density region as did the [Ca II] feature, and yet no comparable wavelength shift is seen in the [O I] feature. (b) The IR echo model indicates an extinction through the outer shell dust of only about $A = 0.15$ mag at 7300 Å. Even allowing for the toroidal geometry, it is not clear that this would be sufficient to account for the profile change. (c) If part of the ejecta/inner CSM impact radiation flowed inwards, it might destroy or inhibit the formation of new ejecta dust. However, it may be that the impact radiation would be severely attenuated by intervening material before it could reach the dust-formation zone. Further discussion of the [Ca II] profile evolution is beyond the scope of this paper. We note that the release in 2009 August of the *Spitzer* observations of SN 2008S at ∼180 d will provide a useful test of the outer shell dust evaporation scenario. We conclude that while the NIR excess provides clear evidence for newly formed dust, the evolution of the [Ca II] feature is somewhat more difficult to explain.

The last phase started after about 120 d when the appearance of the NIR excess indicated the presence of an additional, warm component. The temperature and radius (and therefore the luminosity) of the hot component showed a slower decline during this phase. The warm component cooled from 1400 K at 160 d to 1200 K at about 300 d, while its radius and luminosity increased. An explanation for the NIR excess is thermal emission from newly formed dust in the ejecta or in a CDS formed by the ejecta-inner CSM impact. At this epoch, the decline rate of the SN 2008S light curves flattened to 1.3 to 0 mag/100 d, depending on the band. The bolometric light curve shows a decay rate of 0.88 mag/100 d, very similar to that of ^{56}Co. The velocity width of the broad component and the intensity of Hα declined slower while the velocity width of the intermediate component decreased as in the first phases. The [Ca II]/Hα intensity ratio halved by 260 d while the (Ca II triplet)/Hα declined only slightly. During this later phase, the Na I D and O I appeared in emission.

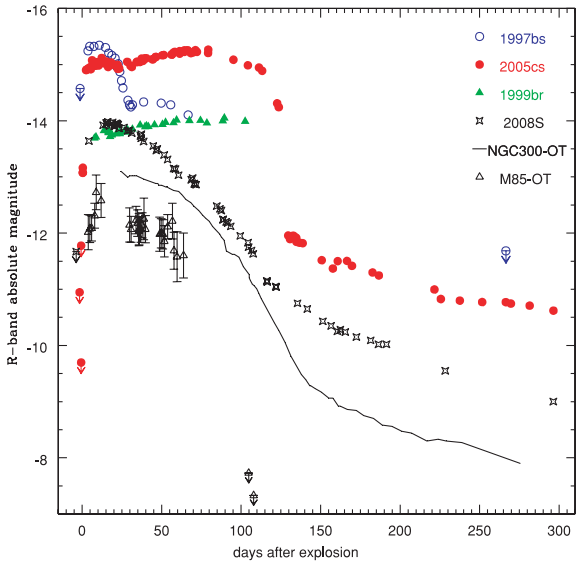

Figure 21. Comparison between light curves of the transients SN 2008S, M85 OT2006-1 (Kulkarni et al. 2007), NGC 300 OT2008-1 (Bond et al. 2009), the subluminous Type II-P SN 1999br (Pastorello et al. 2004) and SN 2005cs (Pastorello et al. 2006; Tsvetkov et al. 2006; Pastorello et al. 2009), and the SN impostor SN 1997bs (Van Dyk et al. 2000).

7.3 Comparison with NGC 300 OT2008-1 and M85 OT2006-1

Several recent papers have suggested an analogy between SN 2008S and two other transients: M85 OT2006-1 (Pastorello et al. 2007; Kulkarni et al. 2007) and NGC 300 OT2008-1 (Thompson et al. 2008; Berger et al. 2009; Bond et al. 2009). The progenitors of the SN 2008S and NGC 300 OT2008-1 transients have been detected only on *Spitzer* pre-explosion images (Prieto et al. 2008b; Thompson et al. 2008; Berger et al. 2009) which indicates very similar properties and geometry of the obscuring CSM. Thompson et al. (2008) have proposed that these transients are members of a new class given the similar pre-explosion properties (see Section 6.3). The extensive multiwavelength monitoring campaigns for both these transients [Smith et al. (2009) and this paper for SN 2008S; Bond et al. (2009) and Berger et al. (2009) for NGC 300 OT2008-1] show that they are indeed very similar in their kinetic and radiative energies. M85 OT2006-1 had a peak R-band absolute magnitude of ~ -12, a peak luminosity $L_{\rm p} \sim 2 \times 10^{40}$ erg s^{-1} and a total radiated energy in the first two months $E_{\rm ph} \sim 6 \times 10^{46}$ erg (Kulkarni et al. 2007), while NGC 300 OT2008-1 had a V-band peak of -13, a luminosity of 1.6×10^{40} erg s^{-1} and a total energy of $\sim 2 \times 10^{47}$ erg and no radio or X-ray emission as SN 2008S (Bond et al. 2009; Berger et al. 2009).

The light curves of both transients are very similar to that of SN 2008S although in the latest phases M85 OT2006-1 faded quickly (Kulkarni et al. 2007), as shown in Fig. 21. In the first phases of its evolution, M85 OT2006-1 showed a warm infrared-bright component likely due to an IR echo by circumstellar dust surviving the explosion (Prieto et al. 2008a). The spectra of both M85 OT2006-1 and NGC 300 OT2008-1 showed Balmer lines, the [Ca II] doublet and the Ca II NIR triplet (Kulkarni et al. 2007; Pastorello et al. 2007; Bond et al. 2009; Berger et al. 2009). Moreover, in NGC 300 OT2008-1 He I (in emission), and Ca H&K and OI λ8446 (in absorption) are visible while M85 OT2006-1 showed also prominent K I lines. The velocity width of Hα is very similar in SN 2008S and NGC 300 OT2008-1, while in M85 OT2006-1 it is narrower.

Smith et al. (2009) have interpreted SN 2008S as an SN impostor analogous to the eruptions of LBVs. They proposed that SN 2008S was a super Eddington outburst of a star of about 20 $M_\odot$, highly obscured because an outburst which had occurred shortly after the recent blue loop transition. However, a 20 $M_\odot$ star has a luminosity of $\log L/L_\odot \simeq 5.0$–5.3 which is not consistent with the total MIR luminosity of the progenitor of $\log L/L_\odot \simeq 4.6$ derived from the analysis of the pre-explosion images. Smith et al. (2009) also suggested that the spectral similarity of SN 2008S in outburst with the hypergiant IRC+10420 points to similar physical conditions of the regions where the emission lines form. The fact that the $T_{\rm eff}$ of the continuum of SN 2008S decreases dramatically, while the emission-line spectrum does not evolve, suggests that the lines are not formed in a stellar like expanding photosphere. IRC+10420, in its quiescent phase, has a luminosity 20 times higher than that of the MIR progenitor but 50 times lower than that of SN 2008S at maximum. Finally, IRC+10420 is not enshrouded by a dusty shell and likely has a different mass-loss history with respect to that of progenitors of these transients. Overall, a physical or evolutionary link between possible LBV-like outbursts and SN 2008S does not seem convincing to us.

In contrast, Thompson et al. (2008) compared the MIR properties of known LBVs in M33 to the progenitors of SN 2008S and NGC 300 OT2008-1 and claimed that an LBV explanation is unlikely for these transients since the LBV luminosity is higher and the LBV MIR colours are much bluer than those of the two transients. Moreover, they stressed that the time-scale of the LBV variability is not consistent with the lack of variability of the MIR progenitors. We would agree that this is evidence against the stellar eruption scenario, at least in any LBV or LBV-like event.

As an explanation for NGC 300 OT2008-1, Berger et al. (2009) and Bond et al. (2009) also favour a stellar eruption which is not unlike that proposed by Smith et al. (2009). But, nevertheless, the issues discussed above still argue against this interpretation for SN 2008S.

Bond et al. (2009) proposed as the SN 2008S-like transient progenitors heavily dust enshrouded luminous stars of about 10–15 $M_\odot$, likely an OH/IR sources, which have begun to evolve on a blue loop towards warmer temperatures. During this transition progenitor stars reached a state in which they exceeded the Eddington limit for their luminosities and masses and suddenly initiated outflows. The reason of these eruptions nevertheless remains uncertain. Berger et al. (2009) explained the nature of NGC 300 OT2008-1 and SN 2008S as an eruption of a blue supergiant or pre-WR star with a mass of 10–20 $M_\odot$ likely in a binary system.

7.4 Comparison with SN 1998S and SN 1979C

The optical light curves of SN 2008S are surprisingly similar to those of Type IIn SN 1998S and Type II-L SN 1979C (Fig. 22), although these were much more luminous [$M_B = -19.6$ from Fassia et al. (2000) and $M_B = -19.4$ from Panagia et al. (1980), respectively]. In the NIR bands, the decline rates of SN 2008S at ~ 170 d after the explosion are similar to those of slowly declining CC SNe templates of Mattila & Meikle (2001) based on SN 1979C and SN 1998S at the same epoch ($J \sim 0.9$ mag/100 d, $H \sim 0.3$ mag/100 d and $K \sim 0$ mag/100 d). In Fig. 22, the *R* band and *UBVRIJHK* quasi-bolometric light curves of SN 2008S are compared with those of SN 1998S, while in Fig. 23 the evolution of the $B - V$, $V - R$ and $V - K$ colours is shown for SN 2008S and SN 1998S. The result of this comparison is intriguing: the overall photometric evolution

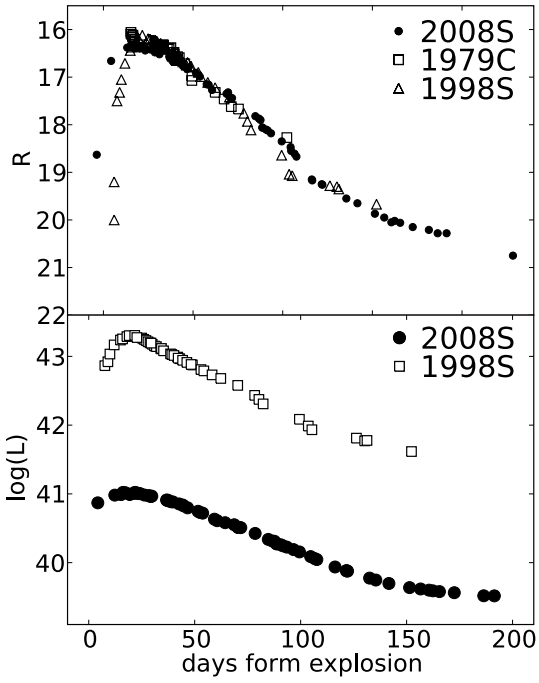

Figure 22. Comparison between light curves of SN 2008S (filled symbols), SN 1998S (empty triangles) (Liu et al. 2000; Fassia et al. 2001) and SN 1979C (empty squares) (Balinskaia, Bychkov & Neizvestnyi 1980; de Vaucouleurs et al. 1981; Barbon et al. 1982): in the top panel the *R*-band light curves (the SN 1998S and SN 1979C light curves are both shifted by 4 mag) and tin the bottom panel the quasi-bolometric light curves of SN 2008S and SN 1998S. Phase is in days after the explosion epoch (JD 245 0869 for SN 1998S, JD 244 3979 for SN 1979C and JD 245 4486 for SN 2008S).

of these events is very similar, the only two differences being the absolute luminosity and a broader peak for SN 2008S.

Hydrodynamical modelling of Type II-L SNe has suggested three quite different evolutionary scenarios and explosion mechanisms. Swartz, Wheeler & Harkness (1991) modelled the collapse of an O–Ne–Mg star, suggesting the electron capture as a mechanism for II-L SNe. Blinnikov & Bartunov (1993) proposed a large supergiant progenitor, while Young, Smith & Johnson (2005) presented a two-component model of a GRB afterglow with underlying SN ejecta. However, there is still not a clear consensus on the bright Type IIn and II-L events such as SNe 1998S and 1979C.

The spectral evolution of SN 1979C and SN 1998S is quite different with respect to that of SN 2008S but there are some common characteristics. Both SN 1979C and SN 1998S showed strong emission lines and absence of P-Cygni profiles during the first months after the discovery (Branch et al. 1981; Fassia et al. 2000). The high density of the CS shell in the case of SN 1998S implies that a CDS forms at the interface of SN ejecta and the CSM. The absence of broad P-Cygni profiles was explained with obscuration by the CDS (Chugai 2001). Fassia et al. (2001) showed that absorption troughs appeared in the spectra of SN 1998S after only 12 d, and suggested that the SN ejecta had over-run the inner CS by that point.

SN 1998S and SN 1979C have been suggested to be the results of explosions of a red supergiant with an extended envelope, $R \sim (1$–$10) \times 10^3\,R_\odot$, and a moderate mass of ejecta $\sim 5\,M_\odot$. Chugai (2001) suggested also that the origin of the CS shell around SN 1998S may be a violent mass loss during the Ne and O burning in cores of $\sim 11\,M_\odot$. The mass-loss rate of the progenitor by optical, radio and X-ray estimates is about 1–$5 \times 10^{-4}\,M_\odot\,{\rm yr}^{-1}$. Likely

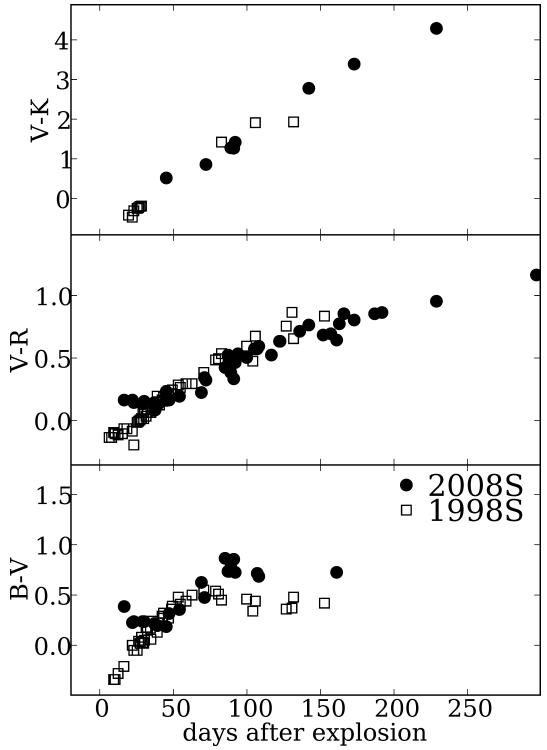

Figure 23. Comparison between $V-K$, $V-R$ and $B-V$ colours of SN 2008S (filled symbols) and SN 1998S (empty symbols). The colours of SN 1998S are corrected for $A_{B,\mathrm{Gal}} = 0.86$ and $A_{B,\mathrm{int}} = 0.09$. Phase is in days after the explosion epoch (JD 245 0869 for SN 1998S, JD 244 3979 for SN 1979C and JD 245 4486 for SN 2008S).

the wind of the SN 1998S and SN 1979C progenitor underwent significant changes in the rate of mass outflow resulting in several distinct CSM shells.

7.5 SN 2008S: an electron-capture SN

An alternative explanation of SN 2008S is the explosion of a massive star in a low, or moderate, energetic SN. We show that the observed characteristics of SN 2008S and its progenitor share characteristics that are common to models of electron-capture supernovae (ECSNe). Such models have been developed extensively in the last three decades. Thompson et al. (2008) suggested that the ECSN was a viable explanation for these SN 2008S-like objects based on the progenitor properties. The energetics of the events and their evolution now add weight to this argument. The strongest evidence for this interpretation is based on the observational discovery that the light-curve tail of SN 2008S follows the decay rate of ^{56}Co. The observation of ^{56}Ni and ^{56}Co decay can be used to distinguish between an SN explosion and multiple shell interaction scenarios (Dessart et al. 2009). The tail phase luminosity decay rate is a strong argument that ^{56}Ni was produced by SN 2008S, and there is no physical channel to produce this radioactive isotope other than explosive burning of oxygen and silicon at temperatures in excess of $\sim 10^9$ K.

A star in the mass range of $\sim$8–10 $M_\odot$ can form an electron degenerate O–Ne–Mg core during the final stage, as it becomes a super-AGB star (Ritossa, García-Berro & Iben 1999; Eldridge & Tout 2004; Siess 2007). Super-AGB stars may end their lives either as massive O–Ne–Mg white dwarfs or as ECSN before Ne ignition (Miyaji et al. 1980; Wanajo et al. 2003, 2009; Nomoto 1984; Hillebrandt, Nomoto & Wolff 1984; Baron, Cooperstein & Kahana 1987; Mayle & Wilson 1988; Poelarends et al. 2008). The final fate of super-AGB stars depends on the competing effects of core growth and mass loss during the late evolutionary stages, particularly during carbon burning. If the core mass reaches the Chandrasekhar mass, high pressure and density lead to electron capture on to ^{24}Mg and ^{20}Ne, the electron degeneracy pressure decreases and the core may collapse before an iron core is formed (Miyaji et al. 1980; Miyaji & Nomoto 1987; Hashimoto et al. 1993; Poelarends et al. 2008; Wanajo et al. 2009). If the mass-loss rate is high enough, the envelope is lost before the core reaches the Chandrasekhar mass and the star ends its life as an O–Ne–Mg white dwarf.

Nomoto (1984, 1987) estimated that stars with a mass of 8–10 $M_\odot$ can become ECSNe but recent work has suggested a more narrow mass range (Siess 2007; Poelarends et al. 2008) and a lower mass limit of $\sim 9\,M_\odot$. However, Podsiadlowski et al. (2004) suggested that the initial mass range may be wider if one considers binary systems, about 8–11 $M_\odot$. ECSNe and their progenitors are predicted to show three properties that might allow us to distinguish them from ordinary CCSNe: they might produce low-energy explosions; the enormous mass-loss rate of the progenitor star in the super-AGB phase may produce signatures of CSM interaction in SN the light curve; the ECSN progenitors have luminosities of the order of $10^5\,L_\odot$ and cool effective temperatures (Eldridge et al. 2007). All these characteristics appear consistent with SN 2008S and its progenitor star. An important implication of the low explosion energy is a small ^{56}Ni mass produced by the explosion. In ECSN explosion models, Kitaura et al. (2006) estimated an explosion energy of 1–2 $\times\ 10^{50}$ erg, an Ni mass of about $10^{-2}\,M_\odot$ and an ejecta velocity after the shock breakout from the stellar surface of $\lesssim$3000 km s^{-1}. The estimated values of energy and ^{56}Ni mass in SN 2008S are somewhat lower than the prediction from Kitaura et al. (2006), but more recent models of ECSNe by Wanajo et al. (2009) are closer to the observed properties of SN 2008S. These weak explosions give an ejected ^{56}Ni mass of 0.002–0.004 $M_\odot$.

The progenitor of SN 2008S is too faint to be a luminous RSG, and too bright to be an intermediate-mass AGB star. It could thus be a super-AGB star or a 'low-mass' (close to $\sim 8\,M_\odot$ also) RSG. One argument in favour of a super-AGB star progenitor is that low-mass RSGs generally do not lose mass fast enough to avoid exploding as a RSG, by far. So they still have massive mantles, but fairly diluted circumstellar envelopes. AGB stars and super-AGB stars lose mass at high rate for longer prior to their ends, which in case of AGB stars means they lose their mantles before core-collapse could occur whereas in super-AGB stars it is a race between mass loss and core growth that determines who wins. The stellar mantle prior to explosion would be thin anyway, one would expect, and the circumstellar medium would be dense. This strong mass loss is an obvious way to account for the optically thick shell around SN 2008S and NGC 300 OT2008-1. Weaver & Woosley (1979) suggested that the super-AGB stars might produce strong flashes in the semi-degenerate core a few years prior to an SN explosion, and the strongest flash could eject most of the H envelope with velocities of $\sim$100 km s^{-1}. The wind speed inferred from the narrow component of Hα (about 200 km s^{-1}), which has likely CSM as origin, has a larger velocity width than is seen normally in AGB stars, although such velocities are not unprecedented in post-AGB stars. Super-AGB stars, or ECSN progenitors, may be distinguished from very massive progenitors of similar luminosity by their much cooler effective temperatures ($\lesssim$3000 K for ECSN versus $\sim$3400 K for CCSN progenitors; Wanajo et al. 2009). The exciting star in the

DUSTY model described above has a temperature of 3000 K, hence consistent with cool super-AGB stars (Eldridge et al. 2007). A lack of α elements in the case of ECSN is also a key to distinguish between the ECSN and CCSNe (Kitaura et al. 2006; Wanajo et al. 2009). It is interesting to note that the Crab remnant has also been suggested to have originated in an ECSN given the low kinetic energy and a small amount of α elements (Nomoto et al. 1982; Chevalier 1984). Moreover, Swartz et al. (1991), as already discussed in the previous section, suggested that the ECSN progenitor may lose a large fraction of their envelope and become a Type II-L SNe.

Finally, the rate of these types of transients would be a useful guide to their physical origins. Wanajo et al. (2009) suggest, from nucleosynthesis arguments, that ECSNe must be $\leq$30 per cent of all CCSN events, while Poelarends et al. (2008) suggest that they should be somewhat rarer ($\sim$7–8 per cent) if they come from a narrow mass range. Thompson et al. (2008) propose that there are possibly four known events that are similar, and that their faint peak magnitudes mean that many more may be undiscovered in the local Universe. The local SN sample compiled by Smartt et al. (2009) shows 92 CCSNe within a local 28 Mpc volume, within a 10.5 yr period. At least, there are four candidates which are SN 2008S-like, as discussed in Thompson et al. (2008). Hence, a lower limit to the rate of these events of $\geq$5 per cent can be inferred, which is not inconsistent with the arguments from theory.

8 CONCLUSIONS

In summary, the combination of our monitoring data and the evidence from the progenitor studies suggests that a weak SN explosion, due to core-collapse through the electron-capture SN mechanism, of a massive star with an initial mass around 6–10 $M_{\odot}$ in the super-AGB stage is a plausible explanation for SN 2008S. By implication, NGC 300 OT2008-1 and M85 OT2006-1 are likely of similar origin. The progenitor star was not a normal RSG which should produce the standard Type II-P SNe (Smartt et al. 2009). However, if the pre-explosion MIR flux reflects the stellar photospheric flux, the object has a luminosity similar to models of super-AGB stars. Extremely high mass-loss rates could create circumstellar shells which are optically thick, cool, dense and dusty (Thompson et al. 2008). Such high mass-loss through thermal pulses has been predicted by theory, and obscured massive oxygen-rich AGB stars are certainly observed by van Loon et al. (2005a).

The evidence that SN 2008S was indeed an SN explosion comes from two observations. First, SN 2008S is similar in the total radiated energy to other faint SNe, and it shows moderate velocities of about 3000 km s^{-1}. The latter are hard to reconcile with either an LBV-like or non-destructive stellar eruption. Secondly, we detect a tail phase which has a decay slope matching that of radioactive ^{56}Co. We estimate the mass of ^{56}Ni ejected to be $0.0014 \pm 0.0003\,M_{\odot}$, which is marginally lower than that observed in the faintest known Type II-P SNe [$\sim$0.002–0.008 $M_{\odot}$ from Turatto et al. (1998), Benetti et al. (2001) and Pastorello et al. (2004)] but is close enough that SN 2008S could be an extension of these low-energy explosions.

Wanajo et al. (2009) have presented models of electron-capture supernovae of progenitor AGB stars with an O–Ne–Mg core and an initial mass of 8.8 $M_{\odot}$ that are in plausible agreement with SN 2008S and similar transients. These weak explosions, as also discussed by Kitaura et al. (2006), give an ejected ^{56}Ni mass of 0.002–0.004 $M_{\odot}$. SN 2008S is also significant in that, apart from SN 1987A, it has allowed the earliest ever MIR observation of an SN, and the remarkably large flux detected confirms the presence of substantial circumstellar material around the progenitor star. In addition, SN 2008S developed an NIR excess at later times. This can be interpreted as optically thin thermal emission from $\sim 10^{-6}\,M_{\odot}$ of amorphous carbon grains or $\sim 10^{-5}\,M_{\odot}$ of silicate grains. However, larger masses of grains, which would be optically thick, are not ruled out. The grain location and heating mechanisms are uncertain. While some of the NIR emission may originate in new, radioactively heated ejecta grains, the magnitude of the later NIR flux requires that at least a proportion must come from an additional source. This might be reverse shock heating of new ejecta grains. Alternatively, it might be due to shock heating of new (CDS) dust or old dust in the circumstellar region.

Our suggested scenario can be tested in the future. If the star has cataclysmically exploded as an SN, then, once the remnant fades, there should be no source left with a luminosity similar to the progenitor ($10^{4.6}\,L_{\odot}$). This needs to be tested over the entire optical to MIR wavelength range to ensure that no progenitor star remains, whether exposed or concealed by newly formed dust. In addition, if the SN ejecta become visible, one might expect to see broad lines of forbidden oxygen (e.g. [O I] $\lambda\lambda$ 6300,6364) and other intermediate-mass elements. This may be difficult, as the events are intrinsically faint, but it could be possible in particular for NGC 300 OT2008-1 as its distance is only 2 Mpc and hence it can be monitored for a long time. The tail phase, following the ^{56}Co decay, should continue at least for another $\sim$300 d, and the slope of this decay should be monitored closely in both SN 2008S and NGC 300 OT2008-1. Finally, the true rate of these transients will give further insights into their nature, and deeper searches by future sky surveys may discover more of these events (Young et al. 2008).

ACKNOWLEDGMENTS

We would like to thank the referee, P. Bouchet, and J. Danziger for helpful discussions and F. Sabbadin for his suggestions on the evolution of line profiles. This work, conducted as part of the award 'Understanding the Lives of Massive Stars from Birth to Supernovae' (S.J. Smartt), done under the European Heads of Research Councils and European Science Foundation EURYI (European Young Investigator) Awards scheme, was supported by funds from the Participating Organisations of EURYI and the EC Sixth Framework Programme. SM acknowledges financial support from Academy of Finland (project 8120503), DT acknowledges financial support from the Program of Support for Leading Scientific Schools of Russian Federation (project NSh.433.2008.2), VS acknowledges financial support from the Fundação para a Ciência e a Tecnologia and IMV acknowledges financial support from SAI scholarship. FPK is grateful to AWE Aldermaston for the award of a William Penney Fellowship. This work is based on observations collected at WHT (La Palma), NOT (La Palma), INT (La Palma), TNG (La Palma), Copernico 1.82 m telescope, the 2.2 m Telescope (Calar Alto). The WHT and INT are operated by the Isaac Newton Group; the NOT is operated jointly by Denmark, Finland, Iceland, Norway and Sweden; the Liverpool Telescope is operated by the Astrophysics Research Institute of Liverpool John Moores University and the TNG is operated by the Fundazione Galileo Galilei – National Institute for Astrophysics (INAF), Fundacion Canaria on the island of La Palma in the Spanish Observatorio del Roque de los Muchachos of the Instituto de Astrofisica de Canarias. The 1.82 m telescope is operated by the Osservatorio di Padova INAF. The 2.2 m telescope is operated jointly by the Max-Planck-Institut fur Astronomie (MPIA) in Heidelberg, Germany, and the

Instituto de Astrofisica de Andalucia (CSIC) in Granada/Spain in the Centro Astronomico Hispano Aleman at Calar Alto. We are grateful to the support astronomers at these telescopes for performing the follow up observations of SN 2008S in particular to P. Rodriguez Gil at Isaac Newton Group of Telescopes, V.P. Goranskij at SAO and T.R. Irsmambetova at SAI Crimean laboratory. Moreover, we are grateful to U. Hopp for arranging the observations at the Wendelstein Observatory, to M. Dolci and E. Di Carlo for arranging observations at Osservatorio di Campo Imperatore and to S. D. Van Dyk and J. Mauerhan for observations at Palomar 5 m telescope. We thank the members of the LBT partnership who contributed to the Science Demonstration Time observation and J. Knapen for the images of the Bok telescope. This work is based in part on archival data obtained with the *Spitzer Space Telescope* and made use of the NASA/IPAC Extragalactic Data base (NED), which are operated by the Jet Propulsion Laboratory, California Institute of Technology under a contract with National Aeronautics and Space Administration. Support for this work was provided by an award issued by JPL/Caltech. We also exploited data products from the 2MASS, which is a joint project of the University of Massachusetts and the Infrared Processing and Analysis center/California Institute of Technology, funded by the National Aeronautics and Space Administration and the National Science Foundation. We acknowledge the usage of the HYPERLEDA data base (http://leda.univ-lyon1.fr).

REFERENCES

Alard C., 2000, A&AS, 144, 363
Arbour R., 2008, CBETs, 1235, 2
Arbour R., Boles T., 2008, Cent. Bur. Electron. Telegrams, 1234, 1
Arnett W. D., Fu A., 1989, ApJ, 340, 396
Balinskaia I. S., Bychkov K. V., Neizvestnyi S. I., 1980, A&A, 85, L19
Barbon R., Ciatti F., Rosino L., Ortolani S., Rafanelli P., 1982, A&A, 116, 43
Baron E., Cooperstein J., Kahana S., 1987, ApJ, 320, 300
Benetti S. et al., 2001, MNRAS, 322, 361
Berger E. et al., 2009, ApJ, 699, 1850
Blinnikov S. I., Bartunov O. S., 1993, A&A, 273, 106
Blondin S., Prieto J. L., Patat F., Challis P., Hicken M., Kirshner R. P., Matheson T., Modjaz M., 2009, ApJ, 693, 207
Bode M. F., Evans A., 1980, MNRAS, 193, 21P
Bond H. E., Bonanos A. Z., Humphreys R. M., Berto Monard L. A. G., Prieto J. L., Walter F. M., 2009, ApJ, 695, L154
Boomsma R., Oosterloo T. A., Fraternali F., van der Hulst J. M., Sancisi R., 2008, A&A, 490, 555
Bouchet P., Danziger I. J., Lucy L. B., 1991, AJ, 102, 1135
Boulanger F., Viallefond F., 1992, A&A, 266, 37
Bowen D. V., Roth K. C., Meyer D. M., Blades J. C., 2000, ApJ, 536, 225
Branch D., Falk S. W., Uomoto A. K., Wills B. J., McCall M. L., Rybski P., 1981, ApJ, 244, 780
Cardelli J. A., Clayton G. C., Mathis J. S., 1989, ApJ, 345, 245
Carignan C., Charbonneau P., Boulanger F., Viallefond F., 1990, A&A, 234, 43
Chandra P., Soderberg A., 2008, Astronomer's Telegram, 1382, 1
Chevalier R. A., 1984, ApJ, 280, 797
Chevalier R. A., Fransson C., 1994, ApJ, 420, 268
Chugai N. N., 2001, MNRAS, 326, 1448
Chugai N. N., 2008, Astron. Lett., 34, 389
Chugai N. N., Utrobin V. P., 2008, Astron. Lett., 34, 589
Danziger I. J., Lucy L. B., Bouchet P., Gouiffes C., 1991, in Woosley S. E., ed., The Tenth Santa Cruz Workshop in Astronomy and Astrophysics, Supernovae Molecules Dust and Ionic Abundances in Supernova 1987A. Springer-Verlag, New York, p. 69
de Vaucouleurs G., de Vaucouleurs A., Buta R., Ables H. D., Hewitt A. V., 1981, PASP, 93, 36
Degioia-Eastwood K., Grasdalen G. L., Strom S. E., Strom K. M., 1984, ApJ, 278, 564
Dessart L., Hillier D. J., Gezari S., Basa S., Matheson T., 2009, MNRAS, 394, 21
Di Carlo E. et al., 2008, ApJ, 684, 471
Drake S. A., Ulrich R. K., 1980, ApJS, 42, 351
Draper P. W., 2000, in Manset N., Veillet C., Crabtree D., eds, ASP Conf. Ser. Vol. 216. Astronomical Data Analysis Software and Systems IX. GAIA: Recent Developments. Astron. Soc. Pac., San Francisco, p. 615
Dwek E., 1983, ApJ, 274, 175
Eldridge J. J., Tout C. A., 2004, MNRAS, 353, 87
Eldridge J. J., Mattila S., Smartt S. J., 2007, MNRAS, 376, L52
Elmhamdi A. et al., 2003, MNRAS, 338, 939
Engargiola G., 1991, ApJS, 76, 875
Fassia A. et al, 2000, MNRAS, 318, 1093
Fassia A. et al., 2001, MNRAS, 325, 907
Gerardy C. L. et al., 2002, ApJ, 575, 1007
Gezari S. et al., 2008, ApJ, 683, L131
Hamuy M., 2003, ApJ, 582, 905
Hamuy M., Pinto P. A., 2002, ApJ, 566, L63
Hashimoto M., Iwamoto K., Nomoto K., 1993, ApJ, 414, L105
Herrmann K. A., Ciardullo R., Feldmeier J. J., Vinciguerra M., 2008, ApJ, 683, 630
Hillebrandt W., Nomoto K., Wolff R. G., 1984, A&A, 133, 175
Junde H., Dailing H., Chunmei Z., Xiaoling H., Baohua H., Yaodong W., 1987, Nuclear Data Sheets, 51, 1
Kamphuis J., Sancisi R., 1993, A&A, 273, L31
Karachentsev I. D., Sharina M. E., Huchtmeier W. K., 2000, A&A, 362, 544
Kitaura F. S., Janka H.-T., Hillebrandt W., 2006, A&A, 450, 345
Knapen J. H., de Jong R. S., Stedman S., Bramich D. M., 2003, MNRAS, 344, 527
Kotak R. et al., 2009, preprint (arXiv:0904.3737)
Kulkarni S. R. et al., 2007, Nat, 447, 458
Lacey C., Duric N., Goss W. M., 1997, ApJS, 109, 417
Langer N., Norman C. A., de Koter A., Vink J. S., Cantiello M., Yoon S.-C., 2007, A&A, 475, L19
Levesque E. M., Massey P., Olsen K. A. G., Plez B., Josselin E., Maeder A., Meynet G., 2005, ApJ, 628, 973
Li H., McCray R., Sunyaev R. A., 1993, ApJ, 419, 824
Liddle A. R., 2004, MNRAS, 351, L49
Liu Q.-Z., Hu J.-Y., Hang H.-R., Qiu Y.-L., Zhu Z.-X., Qiao Q.-Y., 2000, A&AS, 144, 219
Lucy L. B., Danziger I. J., Gouiffes C., Bouchet P., 1991, in Woosley S. E., ed., The Tenth Santa Cruz Workshop in Astronomy and Astrophysics, Supernovae Dust Condensation in the Ejecta of Supernova 1987A – Part Two. Springer-Verlag, New York
Matonick D. M., Fesen R. A., 1997, ApJS, 112, 49
Mattila S., Meikle W. P. S., 2001, MNRAS, 324, 325
Mattila S. et al., 2008, MNRAS, 389, 141
Mayle R., Wilson J. R., 1988, ApJ, 334, 909
Meikle W. P. S., Spyromilio J., Allen D. A., Varani G.-F., Cumming R. J., 1993, MNRAS, 261, 535
Meikle W. P. S. et al., 2006, ApJ, 649, 332
Meikle W. P. S. et al., 2007, ApJ, 665, 608
Miyaji S., Nomoto K., 1987, ApJ, 318, 307
Miyaji S., Nomoto K., Yokoi K., Sugimoto D., 1980, PASJ, 32, 303
Moseley S. H., Dwek E., Silverberg R. F., Glaccum W., Graham J. R., Loewenstein R. F., 1989, ApJ, 347, 1119
Mould J. R. et al., 2000, ApJ, 529, 786
Munari U., Zwitter T., 1997, A&A, 318, 269
Nomoto K., 1984, ApJ, 277, 791
Nomoto K., 1987, ApJ, 322, 206
Nomoto K., Sugimoto D., Sparks W. M., Fesen R. A., Gull T. R., Miyaji S., 1982, Nat, 299, 803
Nugent P. et al., 2006, ApJ, 645, 841
Panagia N. et al., 1980, MNRAS, 192, 861

Pannuti T. G., Schlegel E. M., Lacey C. K., 2007, AJ, 133, 1361
Pastorello A. et al., 2004, MNRAS, 347, 74
Pastorello A. et al., 2006, MNRAS, 370, 1752
Pastorello A. et al., 2007, Nat, 449, 1
Pastorello A. et al., 2009, MNRAS, 394, 2266
Patat F. et al., 2007, A&A, 474, 931
Paturel G., Theureau G., Bottinelli L., Gouguenheim L., Coudreau-Durand N., Hallet N., Petit C., 2003, A&A, 412, 57
Pierce M. J., 1994, ApJ, 430, 53
Pilyugin L. S., Vílchez J. M., Contini T., 2004, A&A, 425, 849
Podsiadlowski P., Langer N., Poelarends A. J. T., Rappaport S., Heger A., Pfahl E., 2004, ApJ, 612, 1044
Poelarends A. J. T., Herwig F., Langer N., Heger A., 2008, ApJ, 675, 614
Pozzo M., Meikle W. P. S., Fassia A., Geballe T., Lundqvist P., Chugai N. N., Sollerman J., 2004, MNRAS, 352, 457
Pozzo M. et al., 2006, MNRAS, 368, 1169
Prieto J. L., Kistler M. D., Stanek K. Z., Thompson T. A., Kochanek C. S., Beacom J. F., 2008a, Astron. Telegram, 1596, 1
Prieto J. L. et al., 2008b, ApJ, 681, L9
Quimby R. M., Aldering G., Wheeler J. C., Höflich P., Akerlof C. W., Rykoff E. S., 2007, ApJ, 668, L99
Ritossa C., García-Berro E., Iben I. J., 1999, ApJ, 515, 381
Roche P. F., Aitken D. K., Smith C. H., 1993, MNRAS, 261, 522
Rouleau F., Martin P. G., 1991, ApJ, 377, 526
Sahu D. K., Anupama G. C., Srividya S., Muneer S., 2006, MNRAS, 372, 1315
Schawinski K. et al., 2008, Sci, 321, 223
Schlegel E. M., 1994, ApJ, 434, 523
Schlegel E. M., 1990, MNRAS, 244, 269
Schlegel D. J., Finkbeiner D. P., Davis M., 1998, ApJ, 500, 525
Schlegel E. M., Blair W. P., Fesen R. A., 2000, AJ, 120, 791
Schmeer P., 2008, Cent. Bur. Electron. Telegrams, 1236, A260000
Schmidt B. P., Kirshner R. P., Eastman R. G., Phillips M. M., Suntzeff N. B., Hamuy M., Maza J., Aviles R., 1994, ApJ, 432, 42
Schoniger F., Sofue Y., 1994, A&A, 283, 21
Sharina M. E., Karachentsev I. D., Tikhonov N. A., 1997, Astron. Lett., 23, 373
Siess L., 2007, A&A, 476, 893
Smartt S. J., Eldridge J. J., Crockett R. M., Maund J. R., 2009, MNRAS, 395, 1409
Smith N. et al., 2007, ApJ, 666, 1116
Smith N., Foley R. J., Filippenko A. V., 2008, ApJ, 680, 568
Smith N. et al., 2009, ApJ, 697, L49
Stanishev V., Pastorello A., Pursimo T., 2008, Cent. Bur. Electron. Telegrams, 1236, 2
Steele T. N., Silverman J. M., Ganeshalingam M., Lee N., Li W., Filippenko A. V., 2008, Cent. Bur. Electron. Telegrams, 1275, A260000
Sugerman B. E. K. et al., 2006, Sci, 313, 196
Suntzeff N. B., Bouchet P., 1990, AJ, 99, 650
Swartz D. A., Wheeler J. C., Harkness R. P., 1991, ApJ, 374, 266
Tacconi L. J., Young J. S., 1990, ApJ, 352, 595
Terry J. N., Paturel G., Ekholm T., 2002, A&A, 393, 57
Thompson T. A., Prieto J. L., Stanek K. Z., Kistler M. D., Beacom J. F., Kochanek C. S., 2008, preprint (arXiv:0809.0510)
Tsvetkov D. Y., Volnova A. A., Shulga A. P., Korotkiy S. A., Elmhamdi A., Danziger I. J., Ereshko M. V., 2006, A&A, 460, 769
Turatto M. et al., 1998, ApJ, 498, L129
Van Dyk S. D., Peng C. Y., King J. Y., Filippenko A. V., Treffers R. R., Li W., Richmond M. W., 2000, PASP, 112, 1532
van Loon J. T., Cioni M.-R. L., Zijlstra A. A., Loup C., 2005a, A&A, 438, 273
van Loon J. T., Marshall J. R., Zijlstra A. A., 2005b, A&A, 442, 597
Wanajo S., Tamamura M., Itoh N., Nomoto K., Ishimaru Y., Beers T. C., Nozawa S., 2003, ApJ, 593, 968
Wanajo S., Nomoto K., Janka H., Kitaura F. S., Mueller B., 2009, ApJ, 695, 208
Waxman E., Draine B. T., 2000, ApJ, 537, 796
Weaver T. A., Woosley S. E., 1979, BAAS, 11, 724
Weiler K. W., van Dyk S. D., Montes M. J., Panagia N., Sramek R. A., 1998, ApJ, 500, 51
Wesson R., Fabbri J., Barlow M., Meixner M., 2008, Cent. Bur. Electron. Telegrams, 1381, 1
Woosley S. E., Blinnikov S., Heger A., 2007, Nat, 450, 390
Wright E. L., 1980, ApJ, 242, L23
Young T. R., Smith D., Johnson T. A., 2005, ApJ, 625, L87
Young D. R., Smartt S. J., Mattila S., Tanvir N. R., Bersier D., Chambers K. C., Kaiser N., Tonry J. L., 2008, A&A, 489, 359
Zwitter T., Munari U., Moretti S., 2004, IAU Circ., 8413, 1

APPENDIX A: DATA TABLES

Table A1. Magnitudes of the local sequence stars in the field of SN 2008S.

ID	*U*	*B*	*V*	*R*	*I*
1	16.41 ± 0.04	16.29 ± 0.04	15.45 ± 0.02	14.97 ± 0.02	14.46 ± 0.05
2	14.56 ± 0.02	14.29 ± 0.02	13.55 ± 0.02	13.13 ± 0.01	12.77 ± 0.02
3	18.35 ± 0.04	17.85 ± 0.03	16.85 ± 0.02	16.30 ± 0.03	15.75 ± 0.03
4	14.77 ± 0.02	14.50 ± 0.02	13.76 ± 0.01	13.34 ± 0.02	12.95 ± 0.03
6	16.83 ± 0.03	16.61 ± 0.03	15.80 ± 0.02	15.32 ± 0.03	14.83 ± 0.02
7	17.94 ± 0.04	17.62 ± 0.04	16.68 ± 0.03	16.16 ± 0.02	15.58 ± 0.02
12	16.79 ± 0.03	16.60 ± 0.02	15.83 ± 0.02	15.37 ± 0.02	14.89 ± 0.01
13	18.41 ± 0.05	17.57 ± 0.04	16.43 ± 0.03	15.75 ± 0.02	15.14 ± 0.02
16	15.87 ± 0.02	15.59 ± 0.02	14.74 ± 0.02	14.27 ± 0.03	13.81 ± 0.03
17	17.88 ± 0.03	17.71 ± 0.04	16.91 ± 0.04	16.45 ± 0.03	15.97 ± 0.03
19	16.13 ± 0.02	15.78 ± 0.02	14.85 ± 0.02	14.34 ± 0.02	13.88 ± 0.02
20	19.89 ± 0.06	18.12 ± 0.05	16.86 ± 0.03	15.99 ± 0.03	15.32 ± 0.03
21	16.75 ± 0.04	16.37 ± 0.03	15.49 ± 0.02	14.99 ± 0.02	14.53 ± 0.02
22	16.55 ± 0.03	16.44 ± 0.03	15.66 ± 0.02	15.21 ± 0.02	14.74 ± 0.02
23		15.56 ± 0.02	13.82 ± 0.03	13.35 ± 0.03	12.91 ± 0.03
26		14.55 ± 0.03	14.38 ± 0.02	13.70 ± 0.02	13.09 ± 0.02

Table A2. Emission features observed on SN 2008S spectra.

Identification	Rest wavelength (Å)	Observed wavelength (Å)	Notes
Hδ	4101	4103	Blend
Fe II (28)	4178.85	4182	Blend
Fe II (27)	4385.38	4387	
Fe II (37)	4472.92	4475	
Fe II (37)	4491	4493	
Fe II (38)	4508.28	4511	Blend
Fe II (37)	4520	4522	
Fe II (38)	4541.52	4543	Blend
Fe II (38)	4549.47	4553	
Fe II (38)	4576.331	4578	
Fe II (38)	4583.829	4586	
Fe II (38)	4620.5	4622	
Fe II (186)	4635.3	4637	
Hβ	4861	4867	Blend
Fe II (42)	4923.92	4926	
Fe II (42)	5018.43	5020	
Fe II (42)	5169.0	5172	
Fe II (49)	5197.56	5199	
Fe II (49)	5234	5237	
Fe II (49)	5254.9	5257	
Fe II (48)	5264.8	5267	
Fe II (49)	5275.99	5277	
Fe II (49)	5316.6	5318	
Fe II (49)	5325.5	5328	
Fe II (48)	5337.71	5340	
Fe II (49)	5425.3	5428	
Na I	5890 5896	5892	
Fe II (46)	5991.38	5995	
Fe II (46)	6084.11	6089	
Fe II (46)	6113.33	6116	
Fe II (74)	6238.38-6239.9	6243	Blend
Fe II (74) + Fe II (92)	6247.55 -6248.89	6250	Blend
[O I]	6300.23	6304	
[O I]	6363.88	6368	
Fe II (40)+ Fe II (93)	6369.5-6371	6372	
Fe II (74)	6416.9	6418	
Fe II (40)+ Fe II (199)	6432.7- 6433.9	6433-6440	Blend
Fe II (74)	6456.38	6456-6461	Blend
Fe II (92)+ Fe II (92)	6491.2 + 6493.035	6492-6496	Blend
Fe II (40)+ Fe II (92)	6516.1 + 6517.0	6519	Blend
H α	6563.5	6568	
[Fe II](14)	7155.14	7159	?
Fe II (73)	7222.39	7226	
Fe II (73)	7224.51	7228	
[Ca II]	7291	7295	
Fe II (73)	7310.24	7313	
[Ca II]	7324	7327	
Mn II (4)	7353.52	7358	?
Mn II (4)	7415.80	7420	?
Mn II (4)	7432.27	7438	?
Fe II (73)	7449.3	7453	Blend
Fe II (73)	7462.38	7465	
Fe II (73)	7515.9	7520	
Fe II (72)	7533.42	7538	
Fe II (73)	7711.71	7716	
Ca II (2)	8498	8505	
Ca II (2)	8542	8547	
Ca II (2)	8662.14	8669	
O I (4)	8446.35		ph 256

This paper has been typeset from a TEX/LATEX file prepared by the author.